FOD in Intakes – A Case Study for Ice Accretion in the Intake of a High Bypass Turbofan Engine

Ahmed F. El-Sayed
*Professor of Aerospace and Mechanical Power Engineering
Zagazig University

www.angelfire.com/ia/afelsayed

1.0 INTRODUCTION

Intake (or inlet) must provide clean and unrestricted airflow to the engine. Clean and undisturbed inlet airflow extends engine life by preventing erosion, corrosion, and foreign object damage (FOD). The idealized assumption of ambient air at rest and with ingestion into the intake uniformly from all sides is not to be found in practice. Due to the vicinity of aircraft components like pylon, wing, and fuselage, deviation from the ideal will result which distort intake air flow. Moreover, atmospheric conditions such as dust, salt, volcanic ash, industrial pollution, foreign objects (birds, nuts and bolts), and temperature (icing conditions) must be made when designing the inlet system. Fairings should be installed between the engine air inlet housing and the inlet duct to ensure minimum airflow losses to the engine at all airflow conditions.

2.0 GROUND AND IN-FLIGHT OPERATION

In many applications of the gas turbine engines, air is frequently laden with solid particles such as sand, dust, and volcanic ashes. Aircraft engines can encounter particles transported by sand storms to several thousand feet altitude. Moreover, for aero-engines (particularly under the wing), sand particles are ingested into the core in many circumstances, during takeoff, landing, climb and cruise conditions. Particles of different sizes are sucked by the intakes during takeoff and landing. Engine inlet to ground vortex during high power setting with the aircraft standing or moving on the runway can blow sand, dust, ice, and other particles into the engine; figure 1. Fortunately, this vortex disappears with the aircraft acceleration. With rear mounted engines, a similar vortex develops (clearly seen if atmospheric condition favor condensation effects) on the fuselage which also disappears as the aircraft takes up speed.

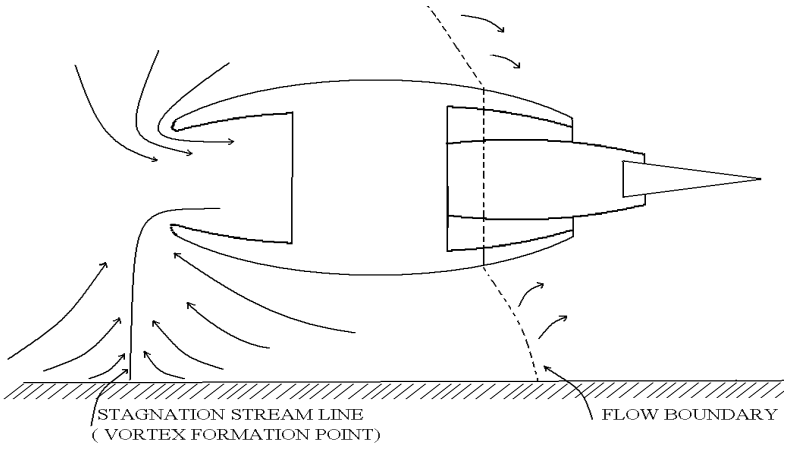

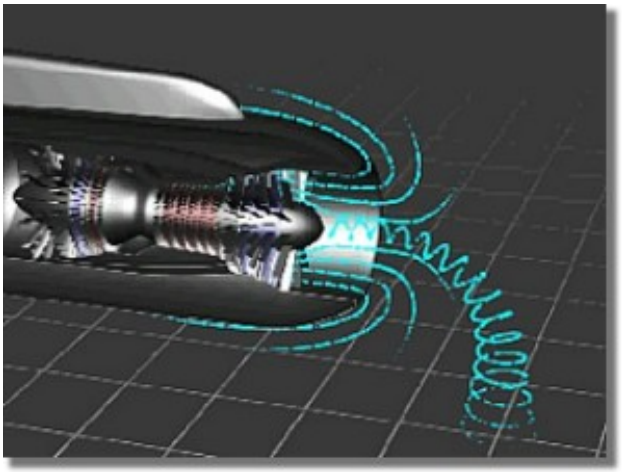

Figure 1: Ground Vortex during ground run.

Moreover, the thrust reversal operation leads to re-ingestion of the hot gases and debris during landing; figure 2.

C-17

Figure 2: Thrust reverse operation.

Helicopter engines are especially susceptible to large amounts of dust and sand ingestion during hover, takeoff, and landing; figure 3. Dust erosion proved so severe during the Vietnam field operations that some engines had to be removed from service after fewer than 100 h of operation [8]. During the Gulf War field

operations, the loss in power and surge margins as a result of compressor blade erosion caused some helicopter units to be removed after fewer than 20 h [9].

Figure 3: Typical Operation of helicopter in desert areas.

Particulate clouds from the eruption of volcanoes present one of the most dangerous environments for aircraft engines; figure 4.

Figure 4: Flight close to erupting volcanoes.

Some airliners are capable for operation from unpaved runways. Examples are Boeing 737 and B 727; figure 5.

Figure 5: Boeing 737 operating from unpaved runways.

Military airplanes operating from air carriers are also vulnerable to ingestion of sea water droplets at takeoff and landing conditions. Figure 6 illustrates F14 while figure 7 illustrates V22 Ospery aircrafts in close sea surface operation.

Figure 6: F14 aircraft operation near sea surface.

Figure 7: V22 Osprey.

Similarly, snow conditions have noticeable effects on performance of aircrafts either during takeoff or landing. Figures 8 and 9 illustrate both airliner and helicopter on operation on and close to ground.

Figure 8: Airliner operation from snow runway.

Figure 9: Helicopter hovering close to snowed ground.

Engines of Seaplanes; which takeoff and land in sea/ocean, are designed to handle air/ liquid droplet suspensions. Figure 10 illustrates Canadair CL-415.

Figure 10: Sea plane Canadair CL-415.

In all the above cases, solid/liquid/ice particles suspended in air are ingested into the engine from outsides. Due to their high inertia they do not follow the carrier phase streamlines and tend to impact the surfaces. Particle-surface interaction causes pitting and cutting of the solid material of either of engine's intake or subsequent modules leading to changes in their geometry and increase their roughness. This will cause changes in the aerodynamic behavior and rapid degradation of the engine performance.

To minimize erosion effects, manufacturer's instructions states that for parked aircraft in an ash cloud environment, it is essential to cover inlets and exhaust openings because ash blowing into the engine will require the same precautionary boroscope inspection procedures as for an aircraft that flew through a volcanic cloud; figure 11.

Figure 11: Covering engine intake for parked aircrafts.

For each aircraft there is a dangerous area which must be clear of personnel/birds and free of any solid equipment to avoid its suction during engine running; figure 12. It is worthy mentioning that:

a) The engine can make enough suction at the inlet duct to pull a person up to, or in to (in part or fully) the duct. This can cause a very bad injury or kill a person.

b) When the thrust reverser operates, the fan air comes out forward. The velocity of the discharge air is sufficiently high to cause a bad injury.

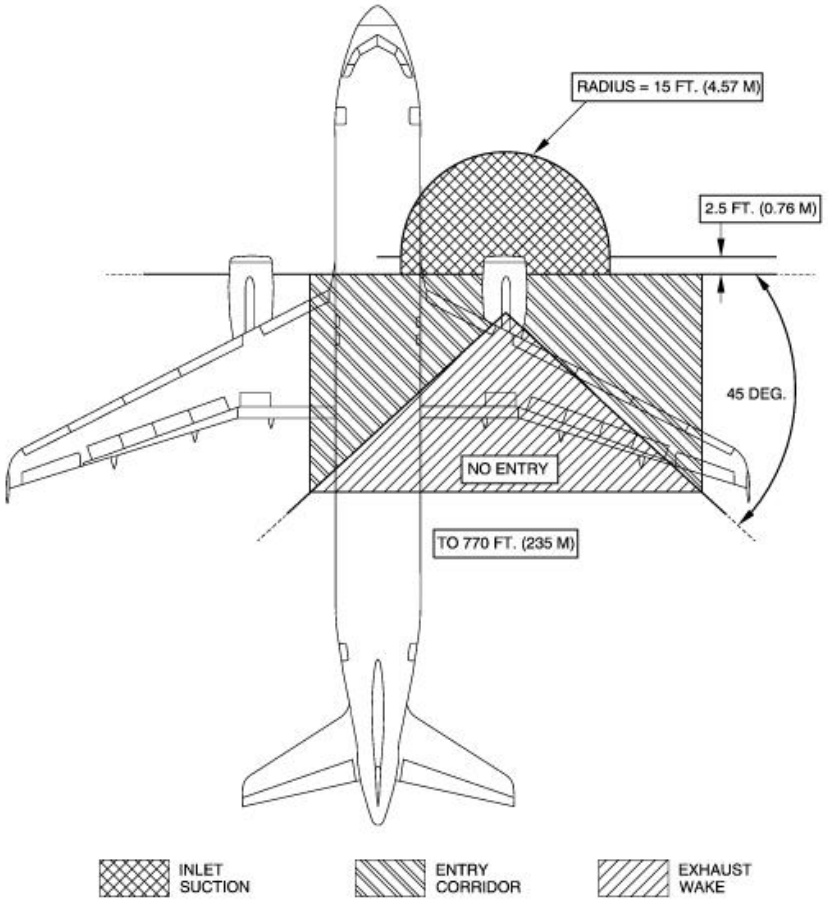

Figure 12: Intake and Exhaust Dangerous Area (A320 aircraft and V2500 engine) Ground Idle.

3.0 FOD

FOD stands for both:

- Foreign Object Debris; and
- Foreign Object Damage.

In aviation, Foreign Object Debris is debris on or around an aircraft or damage done to an aircraft. Foreign Object Damage is any damage attributed to a foreign object (i.e. any object that is not part of the vehicle) that can be expressed in physical or economic terms and may or may not degrade the product's required safety or performance characteristics. FOD is an abbreviation often used in aviation to describe both the damage done to aircraft by foreign objects, and the foreign objects themselves.

As Iain McCreary of Insight SRI put it in a presentation to NAPFI (August 2010), "You can have debris present without damage, but never damage without debris." Likewise, FOD prevention systems work by sensing and detecting not the damage but the actual debris. Thus FOD is now taken to mean the debris itself, and the resulting damage is referred to as "FOD damage".

Though aero-engines are able to lift objects from ground, ingestion is much likely to occur when a particle is already in motion.

This motion may be due to:

1) Jet efflux of another airplane;
2) Thrown by aircraft wheel; and
3) High wind.

The crash of a **Concorde**, **Air France Flight 4590**, at **Charles de Gaulle International Airport** near **Paris** on 25 July 2000 was caused by FOD; in this case a piece of **titanium** debris on the runway which had been part of a **thrust reverser** which fell from a **Continental Airlines McDonnell Douglas DC-10** that had taken off about four minutes earlier. All 100 passengers and nine crew on board the flight, as well as four people on the ground, were killed.

A **Bombardier Learjet 36A**, was taking off from Newport News/Williamsburg International Airport Va., on March 26, 2007, when the crew heard a loud "pop". Aborting the takeoff, the crew tried to control the "fishtailing" and activate the drag chute. The chute did not work and the Learjet ran off the runway, its tires blown. Airport personnel reported seeing rocks and pieces of metal on the **runway**, after the accident. The **NTSB** said that the Learjet accident was caused by Foreign Object Debris (FOD) on the runway. Failure of the drag chute contributed to the accident.

In 2009, on **US Airways Flight 1549**, a Airbus A320 aircraft sucked in one bird in each engine. The plane landed in the Hudson River after taking off from LaGuardia International Airport in New York City. There were no fatalities.

Internationally, FOD costs the aviation industry US$13 billion per year in direct plus indirect costs. The indirect costs are as much as ten times the indirect cost value, representing delays, aircraft changes, incurred fuel costs, unscheduled maintenance, and the like for a total of $13 billion per year and causes expensive, significant damage to aircraft and parts and death and injury to workers, pilots and passengers.

It is estimated that FOD costs major airlines in the United States $26 per flight in aircraft repairs, plus $312 in such additional indirect costs as flight delays, plane changes and fuel inefficiencies.

Examples of (FOD) include:

- Aircraft parts, rocks, broken pavement, ramp equipment, vehicle parts and parts from ground vehicles
- Garbage, maintenance tools, bolts, nuts, metal shavings, lockwire, etc. mistakenly or purposely deposited on tarmac and/or runway surfaces.
- Hail: can break windshields and damage or stop engines.
- Ice on the wings, propellers, or engine intakes
- Dust, sand and ash clogging the air intakes (as in sandstorms in desert operating conditions or ash clouds in volcanic eruptions). For helicopters, this is also a major problem during a brownout.
- Bird Strikes (when an airplane flies into a bird, the impact can cause severe damage from a bird striking the fuselage, engine, etc.). Bird strike is not considered to be FOD strikes, unless the bird or wildlife was already dead and lying on the operating surface when the strike occurred. Bird strikes are treated separately

- Ship deck
- Objects left in intakes during maintenance

Figure 13 illustrates typical FOD.

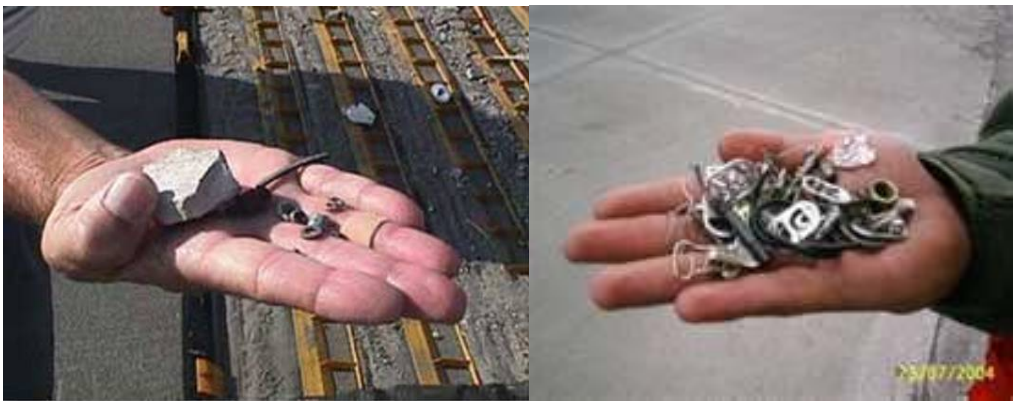

Figure 13: Typical Foreign Object Debris in aviation.

Damage usually occurs when the aircraft is taking off or landing, or when an exhaust jet spraying debris into the intake of a following or parked aircraft. Also, during refueling process foreign objects debris may be ingested into the intake. The intake suction from a jet engine is powerful enough to suck up loose material lying on the runway, and the winds created by a helicopter or prop-driven aircraft's rotors or by a jet blast can send such objects airborne, creating hazards to nearby personnel. One way to counter this is to install a gravelkit, which exist for certain planes like the early Boeing 737

Helicopters (due to their downwash and operation from unprepared sites) and combat aircraft (due to high specific thrust and intake position) are the worst aircrafts affected by FOD>

FOD will fall in one of the following categories:

- Acceptable with no maintenance requirements
- Acceptable with some minor repair (like blending, etc.)
- Unacceptable with either in-site repair or engine removal for shop repair
- Catastrophic, where engine failure leading to either an aircraft incident or accident

FOD screens are installed upstream of the gas turbines in industrial applications (marines) as illustrated in figure 14 for FOD protection. Depending on the screen location and mesh size, the pressure loss across these screens can be negligible or significant.

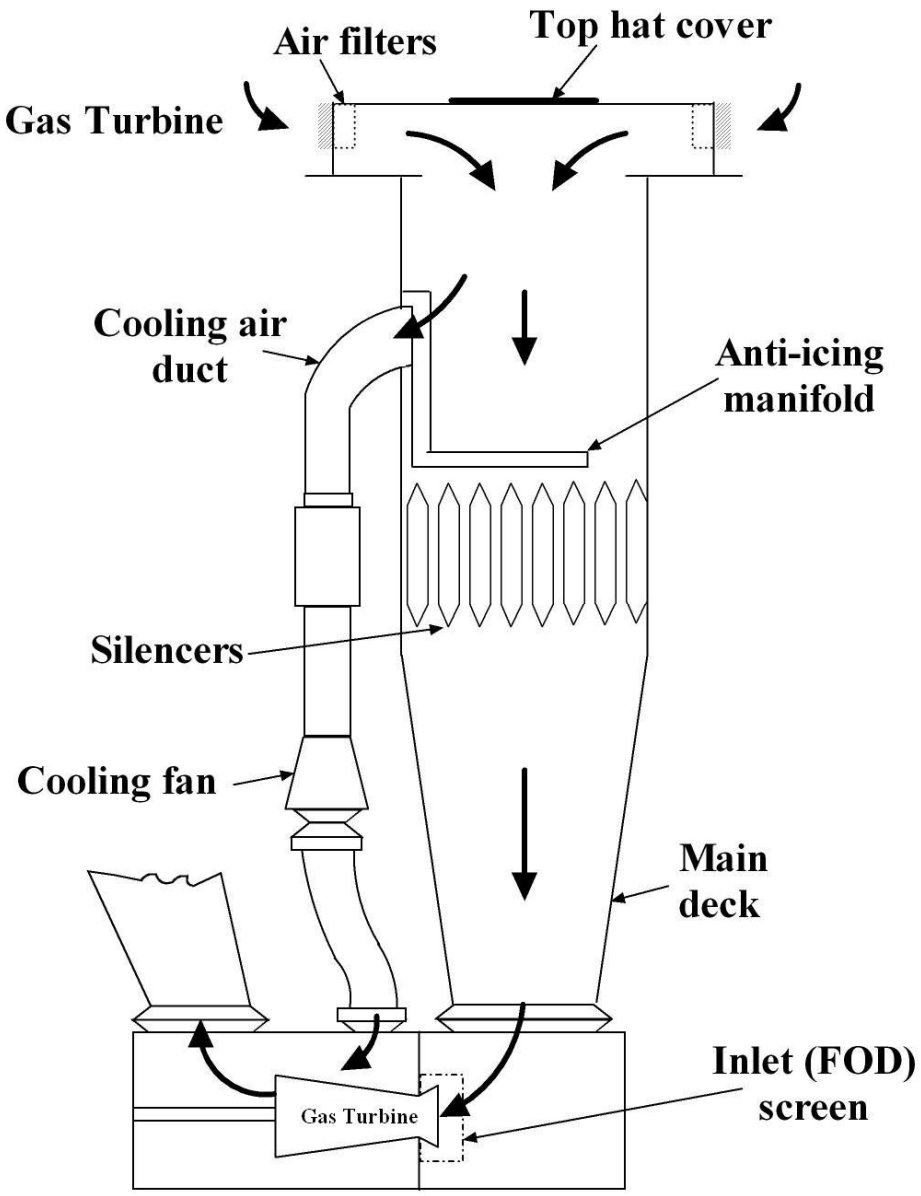

Figure 14: Intake for marine gas turbine fitted with FOD screen.

Engine and airframe designs which avoid FOD:

1) Some military aircraft have a unique design to prevent FOD from damaging the engine. The design consisted of an S-shaped bend in the airflow, so that air entered the inlet, was bent back towards the front of the plane, and bent back again towards the back before entering the engine. At the back of the first bend a strong spring held a door shut. Any foreign object flying in the intake flew in, hit the door, opened it, flew through, and then exited the aircraft. Thus, only small objects swept up by the air

could enter the engine. This design did indeed prevent FOD problems, but the constriction and drag induced by the bending of the airflow reduced the engine's effective power, and thus the design was not repeated. However, many consider it an innovative solution to a challenging engineering problem.

2) The Russian MiG-29 fighter has a special engine design to prevent ingestion of FOD during take-off from rough airfields. The front air intakes could be closed and special inlets on the top of the plane temporarily opened. This would allow enough airflow to the engine for take-off but reduced the chances of the engine sucking up objects from the ground.

3) Another interesting design to minimize the risk of FOD is the Antonov An-74 which has a very high placement of the engines; figure 15.

Figure 15: AN74.

4) Boeing offered a gravel runway kit for early 737s that allows the plane to be used from unimproved and gravel runways. This kit included gravel deflectors on the landing gear; foldaway lights on the bottom of the plane; and screens that prevented gravel, entering the open wheelwells when the gear was extended, from hitting critical components. It also included vortex dissipators, devices that would reduce the airflow into the engine from the bottom so as to reduce the likelihood of ingesting gravel.[10][11]

5) Airbus are investigating a novel approach to reducing FOD. By developing, in conjunction with **Ricardo plc**, the "Taxibot", a tractor controlled by the pilot, aircraft will not need to use jet engines

while taxiing, so will not be vulnerable to FOD on aprons or taxiways. Moreover, it will reduce aviation fuel costs, environmental footprint and ground noise; figure 16.

Figure 16: Taxibot.

3.1 Bird Strike

Significant problems occur with airports where the grounds were or have become nesting areas for birds. Often airports employ a type of **bird scarer** that operates on propane to cause a noise loud enough to scare away any birds that might be in the vicinity. Airport managers use any means available (including **trained falcons**) to reduce bird populations.

Modern jet engines have the capability of surviving an ingestion of a bird. Small fast planes, such as military **jet fighters**, are at higher risk than big heavy multi-engine ones. This is due to the fact that the fan of a high-bypass **turbofan** engine, typical on transport aircraft, acts as a centrifugal separator to force ingested materials (birds, ice, etc.) to the outside of the fan's disc. As a result, such materials go through the relatively unobstructed **bypass duct**, rather than through the core of the engine, which contains the smaller and more delicate compressor blades. **Military aircraft** designed for high-speed flight typically have pure **turbojet**, or low-bypass turbofan engines, increasing the risk that ingested materials will get into the core of the engine to cause damage.

The highest risk of the bird strike is during the takeoff and **landing**, in low **altitudes**, which is in the vicinity of the **airports**.

In-service experience shows that birdstrike events are common. Pilots may expect to encounter from two to five birdstrikes during their career.

The Federal Aviation Administration (FAA), reported over 33000 birdstrikes to civil aircraft between 1990 and 2000. While, from 1990 to 2007, there were nearly 80,000 reports of birds striking non-military aircraft - about one for every 10,000 flights.

Different parts of the world have different levels of exposure to the risk of birdstrike, as shown in Figure 17.

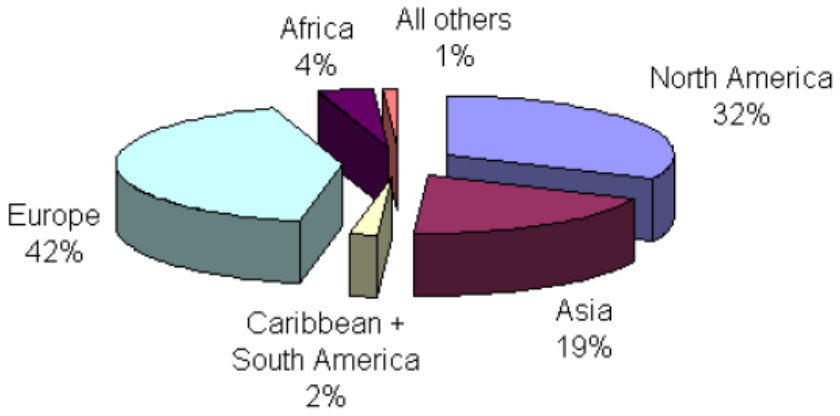

(Source: ICAO)

Figure 17.

Some airports are surrounded by wild life and hundreds of birds may interact with flying aircrafts, figure 18.

Figure 18: Bird strike.

Modern jet engines suffer major damage due to even small birds being sucked into the engine. The FAA (Federal Aviation Administration) requires that all engine types pass a test which includes firing a fresh chicken (dead, but not frozen) into a running jet engine from a small cannon. The engine does not have to

remain functional after the test, but it must not cause significant damage to the rest of the aircraft. Thus, if the bird strike causes it to "throw a blade" (break apart in a way where parts fly off at high speed), doing so must not cause loss of the aircraft. A chicken gun is used to perform experiments on bird strikes

In particular, events linked to the engines revealed that:

a) More than40% of engine birdstrikes damage the engine(s), figure 19

b) When an engine strike occurs and damages the engine, usually:

   − The fan blades are damaged with significant vibrations

   − The EGT increases.

c) Approximately 20 % of engine birdstrikes at takeoff and climb cause an In-Flight Turn Back (IFTB).

d) Approximately 25 % of engine birdstrikes at takeoff result in the flight crew rejecting the takeoff.

e) Only 2% of engine birdstrikes require the flight crew to shut down the engine.

Figure 19: Statistical impact distribution on an aircraft.

Birdstrike Damage

Damage is usually proportional to the bird size and the engine thrust setting.

Small birds such as "starlings", weighing approximately 80 grams (2.8 oz) can cause engine damage especially when at high thrust.

For example, a flock of starlings "*sturnus vulgaris"*, damaged two A340 engines on the same wing, but without thrust loss.

Figure 20: P&W A JT8D after Bird Strike.

3.2 Volcanic Ash

If a jet plane is flying through air densely contaminated with volcanic ash, there is risk of ingested ash eroding the front blades, melting in the combustion heat, and re-freezing sticking to the rear blades, affecting performance and perhaps stopping the engine; as well as triggering long-term corrosion. Figure 21 illustrates a HBPR Turbofan engines subjected to volcano ashes.

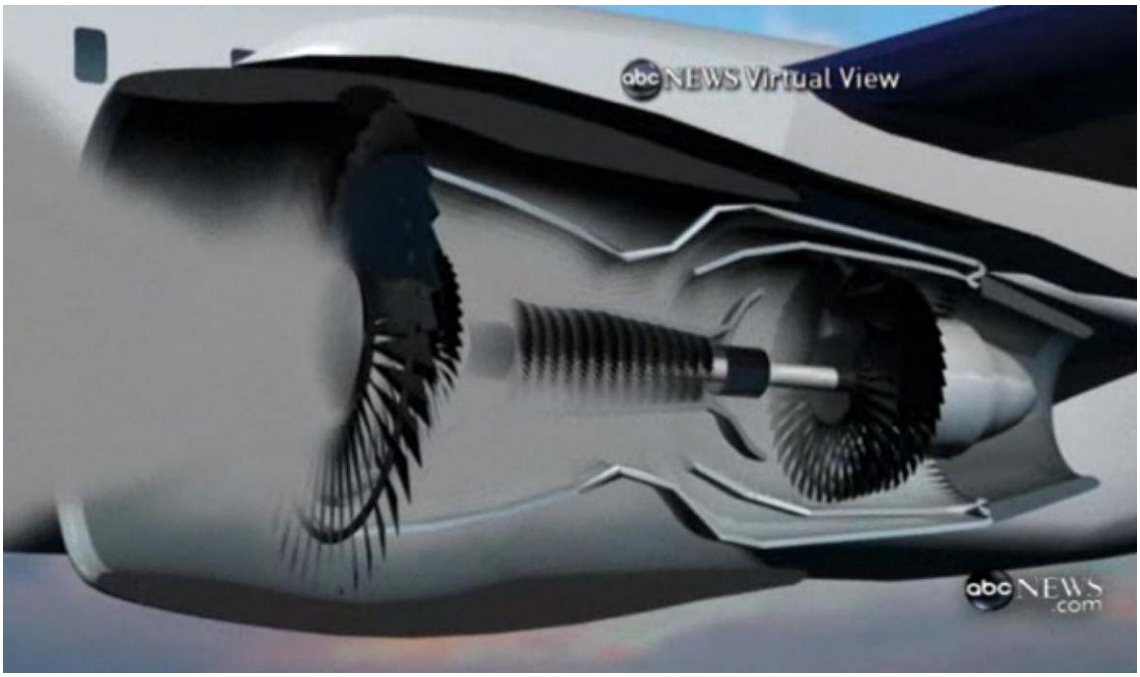

Figure 21: Volcanoes' ashes and HBPR Turbofan engine.

From 1973 through 2000, about 100 encounters of aircraft with airborne volcanic ash have been documented. Aircraft have been damaged by eruptions ranging from small, recurring episodes (e.g., Etna, Italy, 2000) to very large, infrequent events (e.g., Pinatubo, Philippines, 1991). Severity of the encounters has ranged from minor (acrid odor in the cabin and electrostatic discharge on the windshield) to very grave (engine failure requiring in-flight restart of engines). Engine failures have occurred 150 to 600 miles from the volcanic sources. Fortunately, engine failure leading to crash has not occurred. Figure 22 presents a survey for major accidents between 1982 and 1998. Volcanoes are producing lime, rocks and plume. Plume height is between 6-11 km, which is same height of aircraft cruise height, figure 23. It is difficult to differentiate between volcanic clouds and regular clouds neither by eye or radar.

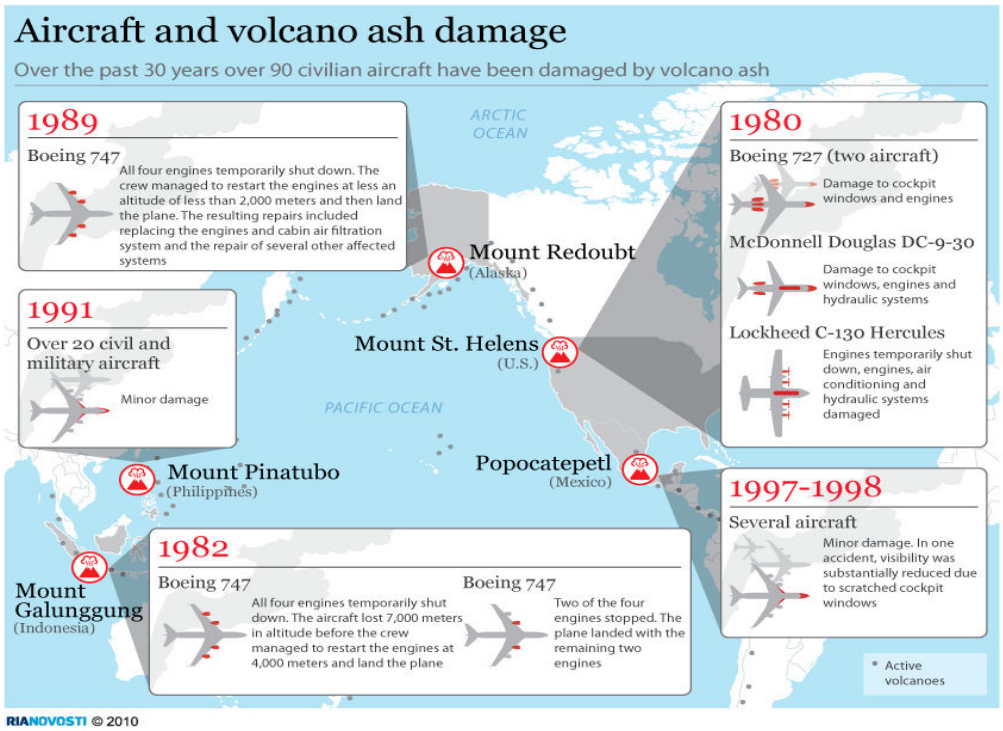

Figure 22: A survey for major accidents between 1982 and 1998.

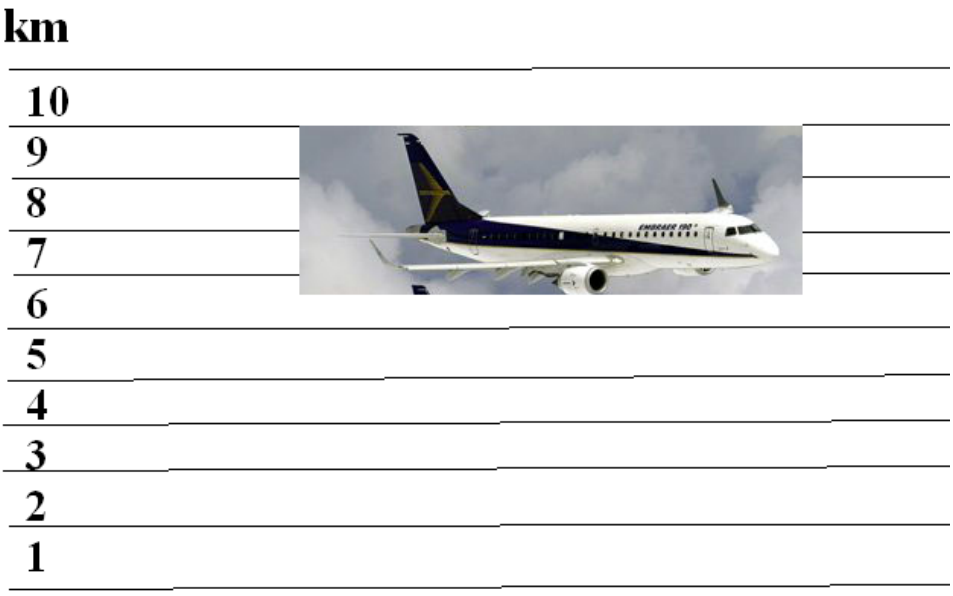

Figure 23: Cruise altitude for present airliners.

2010 Eyjafjallajökull Volcano in Iceland

- Air traffic completely stopped in more than 30 European countries for one week
- It was the biggest shutdown of the continent's airspace for more than 50 years.
- Grounded 100,000 flights in the first 6 days

Figures 24 and 25 illustrate **destructive 2010** Eyjafjallajökull **Volcano in** Iceland.

Figures 24: Tourism near Eyjafjallajökull Volcano.

Figure 25: A *small plane* (upper left) flies past smoke and ash billowing from volcano.

Around 25,000 visitors made a trip by jeep, motorbike and helicopter to see eruption from as close as 200 meters away.

Effects of Volcanoes:

Experimental tests (Dunn and Wade, 1994) determined the following mechanisms that can affect aircraft performance due to exposure to a volcanic ash cloud:

a) Deposition of material on hot-section components.

b) Erosion of compressor blades and rotor-path components.

c) Blockage of fuel nozzles and cooling passages.

d) Contamination of the oil system and bleed-air supply.

e) Opacity of windscreen and landing lights.

f) Contamination of electronics.

g) Erosion of antenna surfaces.

h) Plugging of the pitot-static system which indicates the airspeed of the aircraft

Figure 26 illustrates the damage effects on aeroengine.

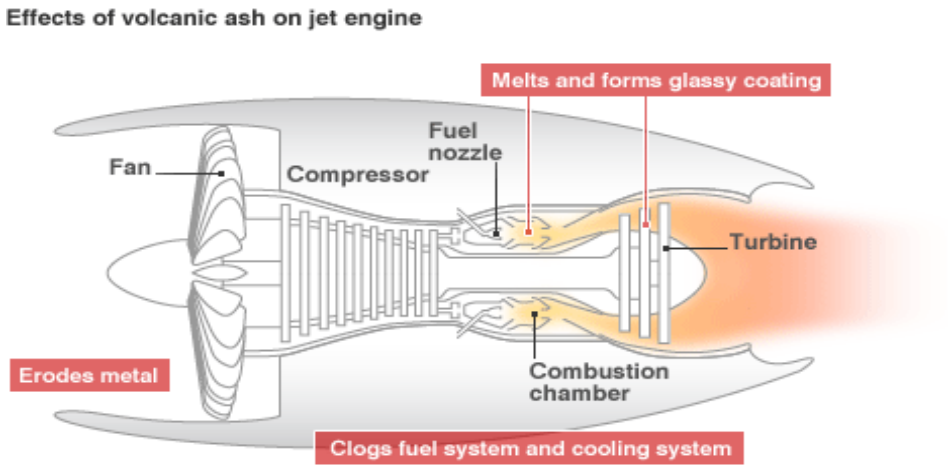

Figure 26: Damage effects on aeroengine.

Figure 27 presents Boeing 747 airplane encountering Mount Galunggung volcano in 24 June 1982.Figure 28 indicates the effect of volcanic ash on both nacelle and nose of turbofan engine

Figure 27: Boeing 747 airplane encountering Mount Galunggung volcano in 24 June 1982.

Crash of DC-10 aircraft after encountering Volcano of Mount Pinatubo in the Philippines, June 15, 1991 is illustrated in figure 29.

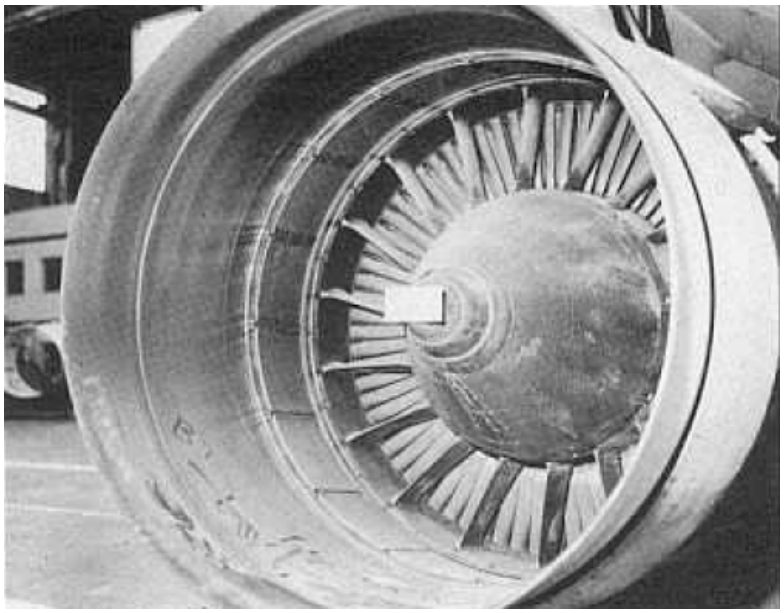

Figure 28: Engine Nacelle and nose cone stripped of paint.

Figure 29: DC-10 crashed due to Volcano of Mount Pinatubo in the Philippines, June 15, 1991.

3.3 Solid Particles

Solid particles may cause erosion or fouling depending on its size as illustrated in figure 30.

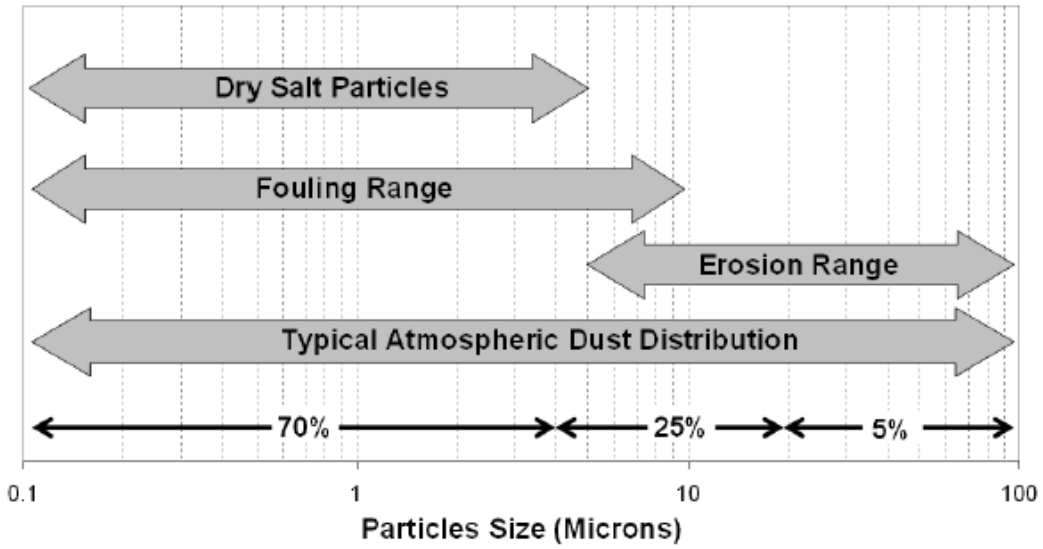

Figure 30: Typical Particles Size Distribution for Erosion and Fouling Range.

Figure 30 compares the particle size range for erosion with fouling. Sand is one of the most common causes of erosion. Impingement of small, hard particles against engine's hardware (intake, rotating and stator blades) repeatedly removes tiny particles of metal, eventually re-shaping portions of the parts. In finely tuned contours of highly stressed parts, this is a double problem. Re-shaping aerodynamic surfaces changes the air flow paths, roughens the surfaces, changes clearances, and eventually reduces the cross-sectional areas that provide the strength necessary to resist the very high stresses of parts with minimal margins of safety. Also, changing the blade shape can create stress concentrations that reduce the fatigue strength, thus leading to high cycle fatigue failures.

Hard particles 5 to 10 microns or larger create erosion of the metal surfaces bounding the air flow path.

Particle ingestion is encountered in either low or high, figure altitudes; figure 31. Low altitude slid particles are ingested due to inlet/ground vortex during high power setting or thrust reverser efflux at low airplane speeds. At high altitudes solid particles are ingested due to either sand storms or volcanic ash.

Figure 31: Operation of V22 Osprey close to ground.

3.3.1 Erosion

The problem of erosion due to particle impact has attracted several researchers to study its mechanism and to know how to control it. The abundant literature on this phenomenon is due to its fundamental and practical importance. But in the case of aircraft's aero-engines, erosion could be a serious problem due to material loss. The erosion rate is defined as the mass removed from a surface per unit mass of particles impinging on the surface. Erosion depends on the time duration, particle impact velocity, impact angle, and the restitution coefficients of the particle-target material combination. Numerous researches focused on obtaining wear data in systems or equipments of practical interest from which erosion relations were derived.

The erosion phenomenon can be classified into two categories namely ductile and brittle erosion. This depends upon the metallurgical properties of the target material. Herein we deal with ductile erosion because the fan alloy is assumed to be a ductile material. As shown in figure 32, the particles act as a cutting tool that removes an amount of mass from the target material.

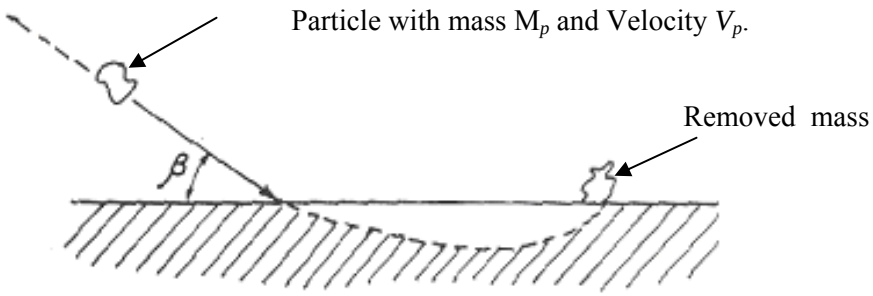

Figure 32: Erosion Pattern for Ductile Material.

Both the impact angle and the impact velocity have the dominant effect on the erosion pattern. Figure 33 shows the effect of the impact angle on the erosion for different target materials. Grant [10] introduced an empirical formula for the erosion per unit mass of impacting particles for different particle and target material combinations. This formula is expressed as follows:

$$\varepsilon = k_1 \, f(\beta) \, V^2 \cos^2 \beta \, (1 - R_T^2) + k_3 \, (V \sin \beta)^4 \qquad (3.1)$$

Where

ε : is the erosion parameter (gm/gm),

V : is the impact velocity (m/s),

β : is the impact angle (degree),

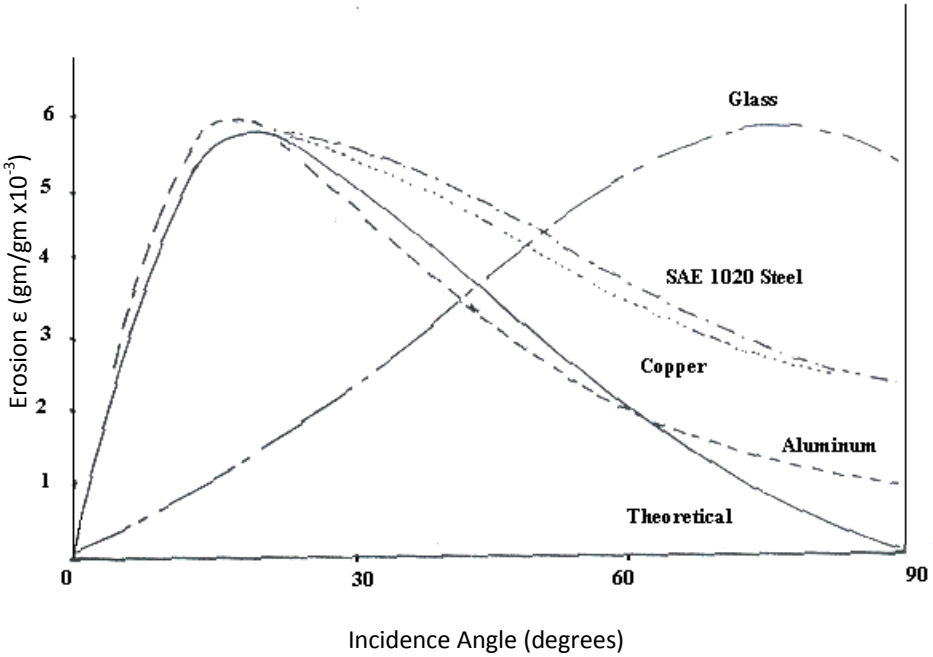

Figure 33: Effect of Impingement Angle on the erosion for different target material.

$$R_T = 1.0 - 0.00525\ V \sin\beta \tag{3.2}$$

$$f(\beta) = 1.0 + CK\ (k_{12} \sin\frac{\pi}{2}\frac{\beta}{\beta_\circ})^2 \tag{3.3}$$

Where

$$CK = \begin{cases} 1 & \beta \le \beta_\circ \\ 0 & \beta > \beta \end{cases}, \quad \beta_\circ \approx 20^\circ$$

β_o is the impact angle at which the maximum erosion occurs. It has a value near 20^0 in case of the ductile erosion. The values for the constants k_1, k_2, k_{12} are determined experimentally for different particles and target material combinations.

Erosion in Turbomachinery

Turbomachinery blade erosion has been the subject of many analytical and experimental investigations by the others. One of the earliest studies was by Montgomery et. al. [11]. He described a test program that was performed to relate the losses in a radial turbine operating life time to the amount and sizes of ingested particles. This study indicated that, particles as small as $2-3\mu m$ can still cause serious losses in the engine operating life time. Extensive studies by Tabakoff et al., [12], Hamed et al. [13], Japikse [14], Wulf et al. [15] related the rate of erosion wear to the time of usage in axial turbomachinery . They claimed that, within 6000 - 8000 hours of jet engine operation, compressor blades had blunt leading edges with an increased surface roughness. The inspection of a new CFM56 turbofan after particle ingestion on its high pressure compressor showed similar effects, Peterson [16].

ElSayed and Brown [17] have also examined erosion phenomenon in axial turbo-machines. They proposed a procedure for evaluating the modified blade shape due to successive impacts of particles in a time-step wise procedure. The first time interval was 2000 hour and successive time intervals followed up to 10,000 hours as a suggested time for hot section inspection or overhaul. Clevenger and Tabakoff [18] treated the particulate flow problems in radial inflow turbines. ElSayed and Rashed [19] and [20] investigated the air flow and the erosion rate of centrifugal compressors. They estimated the lifetime of centrifugal compressor due to successive operation in polluted environment or sandy areas.

Elsayed and Rouleau [21] investigated the erosion of stationary cascades in turbo-expanders. The air flow velocities were measured in many points within the passage using LDV. Next, the particle trajectories were calculated numerically. The change of the aero-elastic behavior was examined by Elsayed Abdelazim [22]. Zoheir [23] predicted the erosion rate due to sand particles on the fan blade numerically. Elsayed, et.al, examined erosion damage of axial fan of a HBPR turbofan engine due to sand particles ingestion [24]. Dunn, et al. [25] examined performance deterioration of a turbofan and a turbojet engine upon exposure to a dust environment.

3.3.2 Fouling

Fouling is defined as the accumulation of deposits on target surfaces causing an increase in surface roughness. This is caused by the adherence of particles to airfoils and annulus surfaces due to the presence of oil are

water mists. The result is a buildup of material that causes increased surface roughness and to some degree changes the shape of the airfoil. Fouling is mainly caused by dust particles of about 2 micron and less in diameter which are not removed by filters. Foulants in the parts per million (ppm) range can cause deposits on balding, resulting in severe performance deterioration. Normal operation of an engine, even if it is equipped with a good filter, results in accumulation of dirt, dust, pollen, insects, tree sap, etc. particles on the compressor airfoils and gas path surfaces, as well as blocking of the inlet filters. The degree of fouling, the rate of fouling, and the effect on performance depend on many factors including surface smoothness/coating, type and condition of the airborne contaminates, the site environment, and the climate conditions (high humidity increases the rate of fouling).

3.4 Rain and Snow

The biggest danger posed by forms of precipitation like rain, snow, ice, or fog is an engine flameout. A flameout is defined as a loss of engine power that is not caused by a mechanical failure. The majority of storms produce light rain or snow that has little if any impact on an engine. Clouds are also made of small ice crystals that have no appreciable effect. Even in a strong storm, however, the main consequence a jet engine experiences is a reduction in the efficiency of the combustion process. This efficiency is a function of the fuel-air ratio that is changed by the presence of water vapor. This effect is negligible under most conditions since the percentage of water present in the large volume of air entering an engine is still relatively small in most storms. Intense rain or hail can cause the combustor to burn the air-fuel mixture less efficiently. Usually this effect is negligible because the intense period of a storm is generally brief.

Many turbofan engines also take advantage of their bypass air system to remove precipitation from the airflow before it reaches the combustion section. As the incoming air moves into the rotating fan blades, the spinning motion flings the heavier water outward like a centrifuge. The water is then blown through the bypass air ducts that surround the engine core. In this way, the water is carried through the engine without ever entering the combustion chamber.

3.5 Ice Accretion

Aircraft and aero-engines can accrete ice on its aerodynamic surfaces when flying through clouds of super-cooled water droplets. The size and shape of the ice accretion on unprotected aerodynamic surfaces depend primarily on airspeed, temperature, water droplet size, liquid water content, and the period of time the aircraft has operated in the icing condition.

Under a normal icing encounter, most of the ice accretion would occur over the engine nose and lips as well as active portion of the wing deicing system. Figure 35 illustrates severely iced aircraft and engines.

Figure 35: Severe ice accretion of aircraft and engines.

High-altitude ice crystals in convective weather are a cause of engine damage and engine power loss that affects multiple models of commercial airplanes and engines. The engines in all events have recovered to normal thrust response quickly. Research is being conducted to further understand these events. Normal thunderstorm avoidance procedures may help pilots avoid regions of high ice crystal content.

NASA Glenn since several decades developed both experimental and computational facilities to investigate ice accretion problem. This includes icing wind tunnel and code LEWICE. The main structure of code LEWICE is illustrated in figure 36.

Figure 36: LEWICE CODE STRUCTURE.

Since 1990, there have been at least 100 jet engine power loss events on both commuter and large transport airplanes, mostly at altitudes higher than 22,000 feet, the highest altitude where airframe icing is expected to

exist. "power loss" is defined as engine instability such as a surge, stall, flameout, or rollback that results in a sub idle operating condition. High altitude ice crystals are believed to have caused most or all of these events.

High-Altitude Ice Crystal Icing

Several engine power loss and damage events have occurred in convective weather above the altitudes typically associated with icing conditions. Very small ice crystals, perhaps as small as 40 microns (the size of flour grains), can affect an engine when flying through convective weather.

Ice building up on the inlet, fan, or spinner would likely shed outward into the fan bypass duct without causing a power loss. Therefore, in these powerloss events, it is reasonable to conclude that ice must have been building up in the engine core. It is now believed that ice crystal icing can occur deep in the engine where surfaces are warmer than freezing, figure 37.

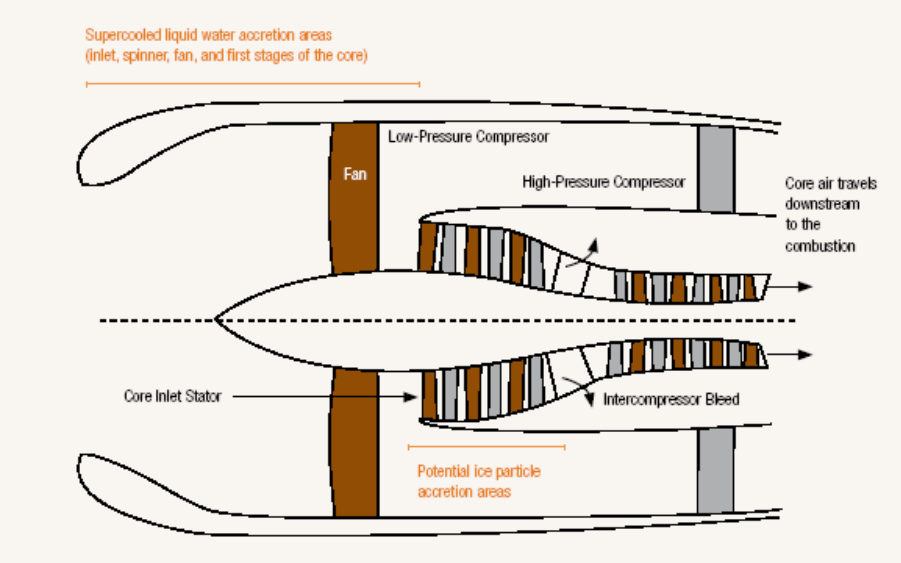

Figure 37: Ice accretion locations for turbofan engines.

About 60 percent of recorded ice crystal power loss events [26] have occurred in Asia, figure 38.

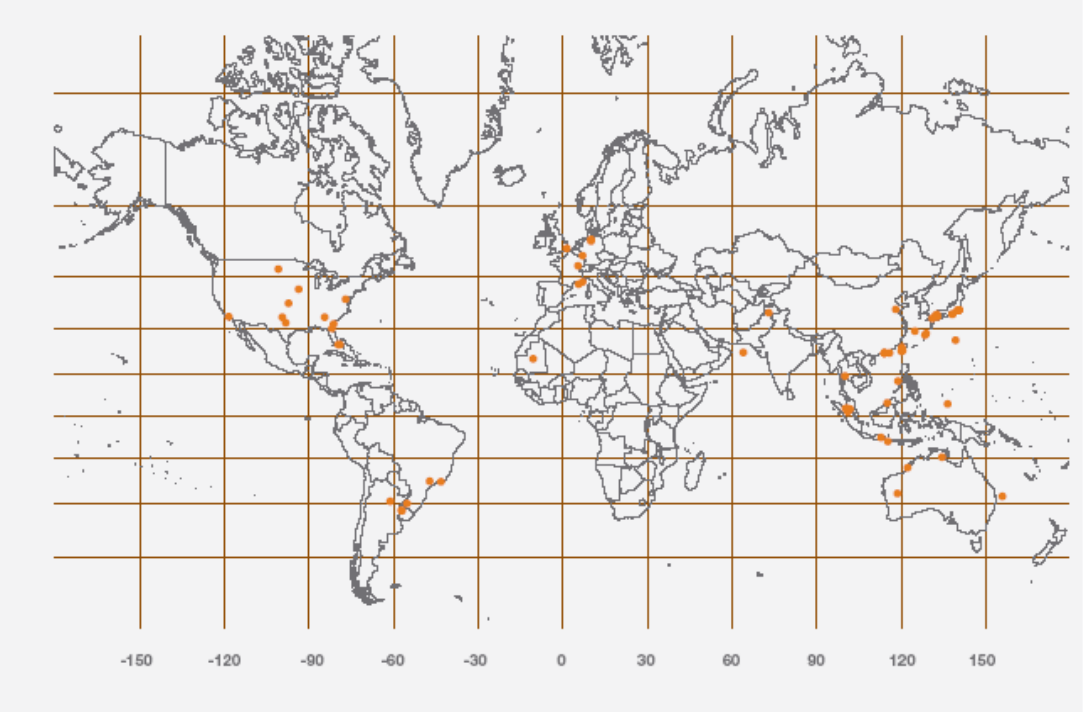

Figure 38: Location of most power loss events.

Commercial airplane powerloss events associated with ice crystals have occurred at altitudes of 9,000 to 39,000 feet, with a median of 26,800 feet, and at ambient temperatures of –5 to –55 degrees C with a median of –27 degrees C. the engine powerloss events generally occur on days when the ambient temperature is warmer than the standard atmosphere; figure 39.

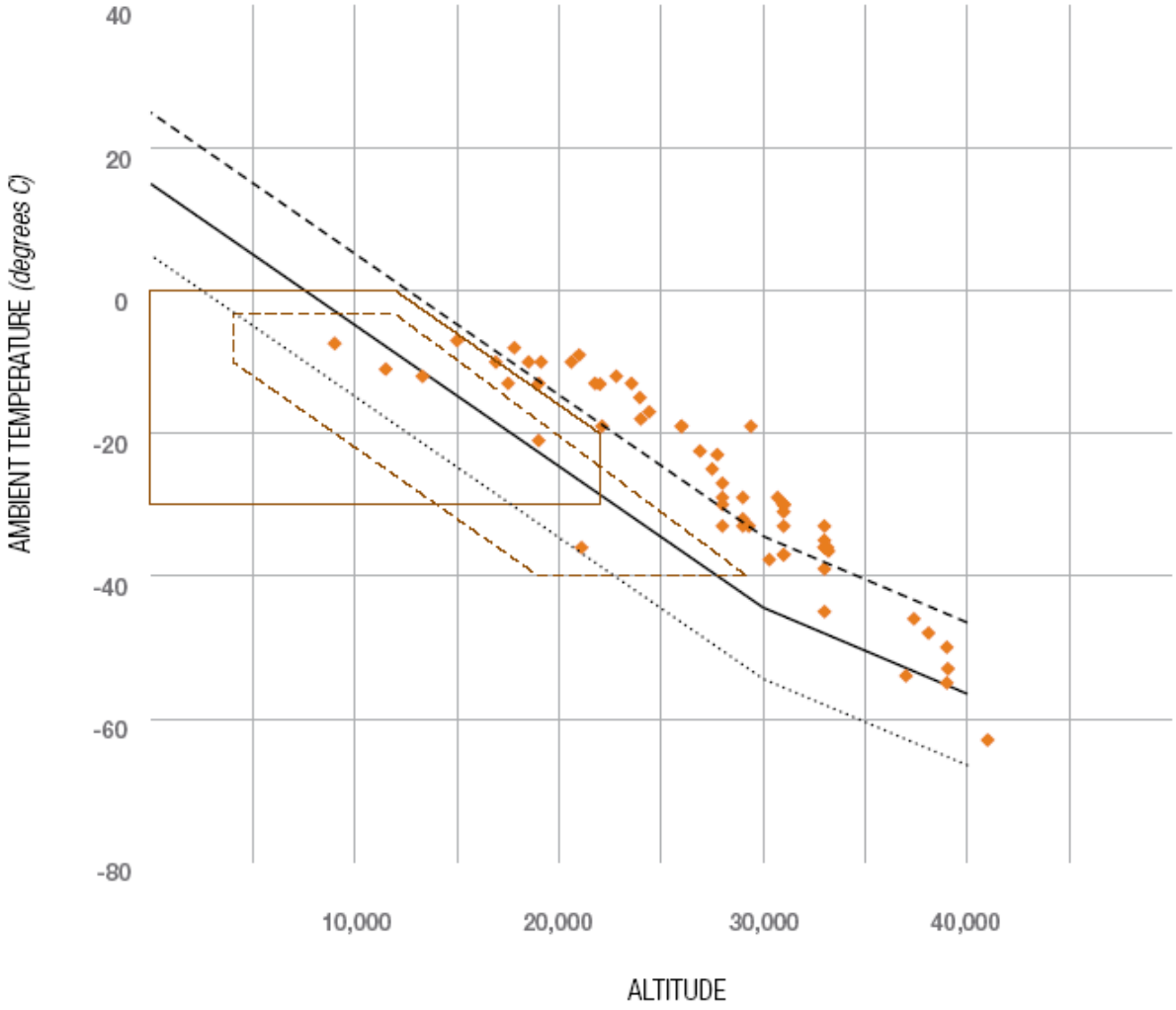

Figure 39: Altitude and temperature of power loss events of commercial airplanes.

4.0 CASE STUDY

Icing of Intake of HBPR Turbofan Engine

4.1 Introduction

The intake of an aircraft engine is an important component which affects not only the propulsive characteristics but also the aerodynamic characteristics of the aircraft. The intake delivers the free stream air to the engine in different flight phases. It retards the incoming flow and converts its kinetic energy into pressure. Although it does not do any work on the flow itself, it is responsible for the quality of the air at the face of the fan /compressor of any aero-engine.

Ice accretion of the intake (inlet) of a high bypass ratio turbofan HBPR engines (like CF6, CFM56, V2500, PW4000 and Trent engines), when passing through clouds, is investigated here.

Modeling process is carried out through three successive steps;

1) Calculating air flow properties around and inside intake
2) Tracing trajectories of supercooled water droplets starting from specified points at air far field upstream of intake
3) Calculating the collection efficiency and the rate of ice accretion for particles colliding with intake surface

Air flow is numerically investigated, using the commercial fluent package FLUENT 6.0. Both of continuity, Navier-Stokes, and energy equations are coupled together and solved. Spalart-Allmaras turbulence model is used. For computational purposes, a three dimensional sector having an angle of 15^{o}, including the intake and the external domain around the intake is employed due to the limited computational facilities. For several flight and operating conditions, the intake aerodynamic characteristics (Mach number, static pressure, static temperature, drag coefficient) are obtained and studied.

For particle dynamics, super-cooled water droplets of different sizes are traced from specified initial points upstream the intake. It is assumed that these droplets have the same initial conditions (velocity and temperature) as the air at such particular point. FLUENT code solves the equation of motion for each droplet to predict its trajectory with the aid of user defined function.

When impacting the intake surface, ice builds up within a certain time step. The geometry of intake is successively changing due to ice accretion. An iterative procedure is followed up then. The new intake geometry is specified, the anew airflow pattern is computed and the resulting particle trajectories are traced. Finally, the new impingement characters and collecting efficiencies are defined. The previous procedure is repeated for a total cumulative time of 20 minutes.

Influence of ice accretion on both pressure recovery factor, air mass flow rate and drag coefficient of intake are defined as function of altitude, Mach number and water droplet size.

Five different flight Mach number (0.3, 0.4, 0.6, and 0.8) and four different altitudes, (10680, 8461.5, 7000, 5000 meters) are examined.

The results show that the flow characteristics are just a function of the flight Mach number and mass flow parameter and independent of the altitude.

4.2 Air Flow

The governing equations "continuity, momentum and energy", are used to solve the air flow upstream and inside the intake. Spalart-Allmaras turbulence model is utilized to simulate the real air flow. A computational domain is generated around the intake; at least six time the intake diameter at the fan face. A 3-dimensional sector of 15^{o} is selected to generate the mesh. Hexagonal elements are employed with a moderate skewness ratio to accelerate the convergence of the solution. The boundary types are chosen carefully to simulate the ambient conditions and flight Mach number. These boundary conditions are static pressure and static temperature at the far field equal to the local ambient condition. The fan boundary condition is expressed as a certain mass flow rate through the intake outlet. This mass flow rate is determined from the performance map

of the fan. The obtained mass flow rate is substituted in the gas flow dynamic relations to obtain the static pressure at the intake outlet that expresses the corresponding mass flow rate.

4.2.1 Governing Equations

The basic governing equations for a steady viscous flow namely, conservation of mass or continuity equation, conservation of momentum, and conservation of energy are described here after.

Mass Conservation (Continuity Equation)

The steady compressible continuity equation can be written as

$$\frac{\partial}{\partial x_i}\left(\rho V_i\right)=0 \tag{4.1}$$

Momentum Conservation Equations

Conservation of momentum (Navier-Stokes equations) in an inertial reference frame is,

$$\frac{\partial}{\partial x_j}\left(\rho V_i V_j\right)=-\frac{\partial P}{\partial x_i}+\frac{\partial \tau_{ij}}{\partial x_j} \tag{4.2}$$

$$\tau_{ij}=\mu\left[\frac{\partial V_i}{\partial x_j}+\frac{\partial V_j}{\partial x_i}-\frac{2}{3}\delta_{ij}\frac{\partial V_l}{\partial x_l}\right] \tag{4.3}$$

Energy Equation

$$\frac{\partial}{\partial x_i}\left[V_i\left(\rho E+P\right)\right]=\frac{\partial}{\partial x_i}\left(k\frac{\partial T}{\partial x_i}+V_j\tau_{ij}\right) \tag{4.4}$$

The first term in the right hand side of equation (4.4) represents the convection through air, while the second term represents the heat generated due to viscous shear in the flow. Air total energy is given by the following equation

$$E=\mathrm{e}+\frac{\mathrm{V}^2}{2} \tag{4.5}$$

Turbulence Model

The Spalart-Allmaras model is a relatively simple one-equation model that solves a modeled transport equation for the kinematic eddy (turbulent) viscosity. This embodies a relatively new class of one-equation models in which it is not necessary to calculate a length scale related to the local shear layer thickness.

In FLUENT code, the Spalart-Allmaras model has been implemented to use wall functions when the mesh resolution is not sufficiently fine. This might make it the best choice for relatively crude simulations on coarse meshes where accurate turbulent flow computations are not critical.

Methodology

For simplicity, the studied subsonic intake is assumed to have circular inlet geometry. Figure 40 shows the main dimensions of this intake. Here it is required to study air flow field at different operating conditions (flight Mach number and altitude). This necessitates a huge computational domain; or a large number of cells. Assuming an axi-symmetric flow, a three dimensional 15^{o} degree sector is selected to represent the computational domain (other sectors are assumed to be a repeating periodic sections); figure 41. The computational domain is six times the fan diameter in the axial and radial directions (Five times the diameter in front of the intake and above it three times the diameter); figure 42. The fluent pre-processor called "GAMBIT" is employed in mesh generation. Hexagonal elements are used due to its stable convergence criterion as shown in figure 43.

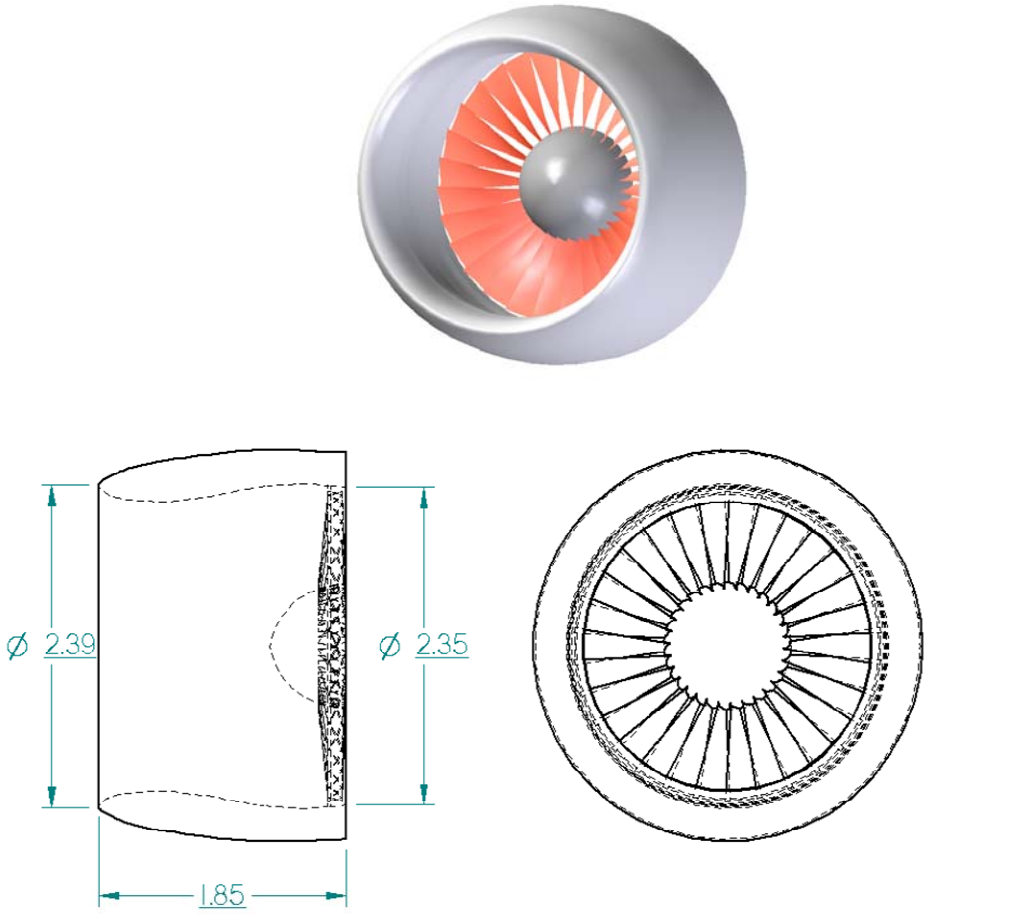

Figure 40: Intake dimensions.

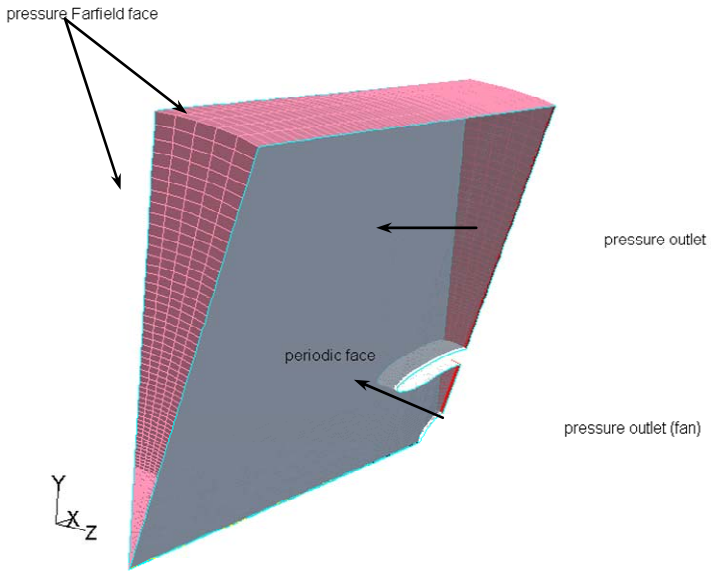

Figure 41: Schematic Diagram of Computational Domain.

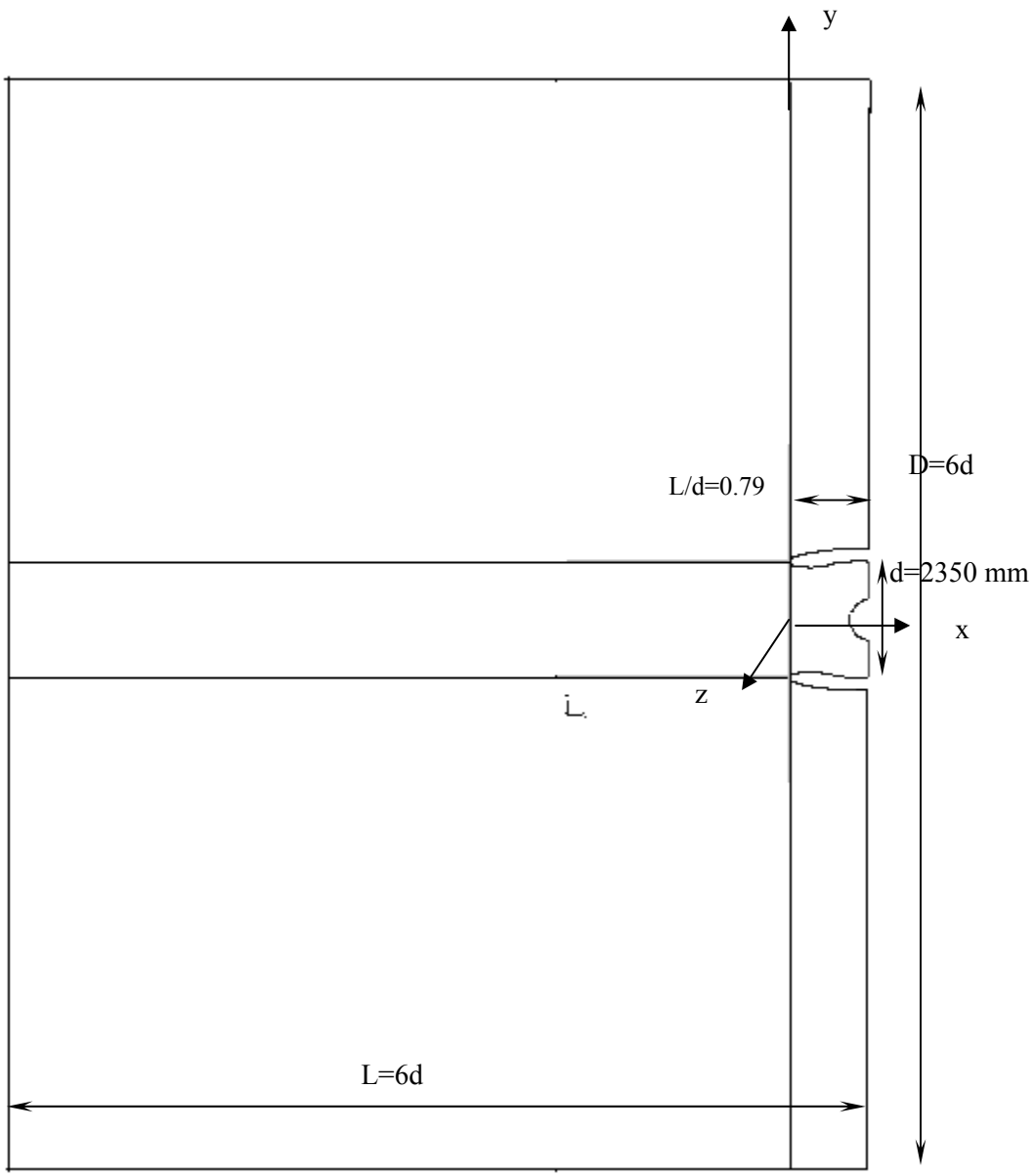

Figure 42: Overall dimensions of the computational domain.

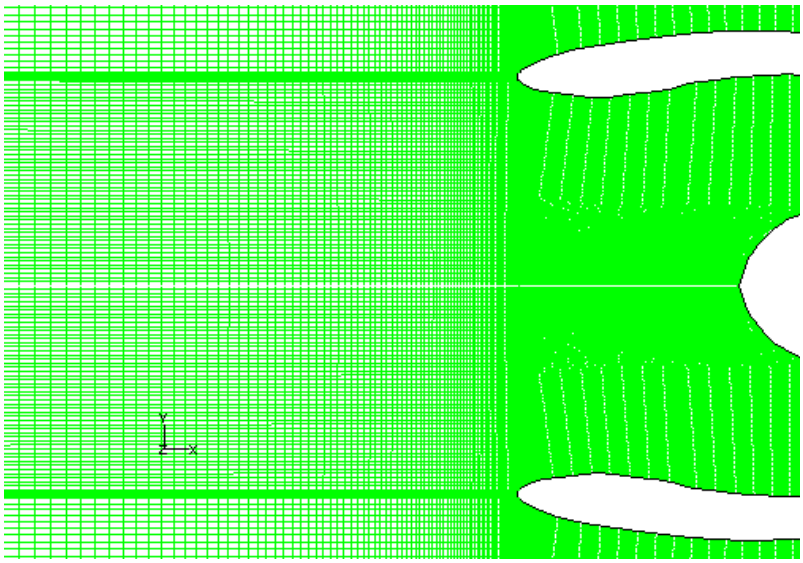

Figure 43: Section view in the hexagonal mesh of the computational domain.

Table 1 shows the number of cells, faces, and nods generated.

Table 1: Number of cells in each sub-domain.

Number of cells	325420
Number of faces	992346
Number of nods	369961

Boundary Conditions

The boundary conditions are the ambient static pressure, ambient static temperature and Mach number for the "far field" boundary type. In addition the boundary conditions are the ambient static pressure and total temperature for the "pressure-outlet" boundary type. The fan is simulated herein by a "pressure-outlet" boundary type to simulate the actual mass flow rate of air for certain flight condition. It is determined by trial and error from the fan performance map and the dimensionless mass flow parameter; equation (4.6), to calculate the corresponding Mach number; the static pressure and temperature at fan inlet. The nacelle is simulated by defining it as a constant temperature wall which has the same ambient static temperature of the far field, while the hub has the same average static temperature of the air flow around it.

$$\frac{\dot{m}\sqrt{T_0}}{AP_0}\sqrt{\frac{R}{\gamma}} = \frac{M_{fan}}{\left(1+\frac{\gamma-1}{2}M_{fan}^2\right)^{\frac{\gamma+1}{2(\gamma-1)}}} \tag{4.6}$$

Table 2 lists all boundary conditions.

Table 2: The boundary types and the required input

Boundary	Boundary type	Input
Fan	Pressure outlet	Static pressure Total temperature
Hub	Wall	Constant surface temperature
Nacelle	wall	Constant surface temperature
Domain outlet	Pressure outlet	Static pressure Total temperature
Far field	Farfield	Mach number Static pressure (ambient) Static temperature (ambient)

4.2.2 Air Flow Results

The flow characteristics are investigated at different flight conditions (i.e. Altitude and flight Mach number) and fan rotational speed. Any combination of these boundary conditions gives certain mass flow rate through the intake. For certain flight condition, the static pressure is calculated to achieve certain mass flow rate through the intake (corresponding to certain fan speed). To make the investigation more realistic, a BASIC computer program developed by Gobran [1] is used to calculate the off-design performance of a high by-pass turbofan engine (similar to CF-6) by assuming flight condition and fan speed, as a base line parameter. The fan mass flow rate is one of the calculated off design parameters. By knowing the fan air mass flow rate, the fan inlet static pressure is determined from the gas dynamics. Table 3 gives typical values for fan mass flow rate corresponding to different flight and operating conditions and fan inlet static pressure.

Table 3: Input values for some cases study.

Case	Operating conditions			Mass flow rate (kg/s)	Static pressure at fan inlet (Pa)
	Flight conditions		Fan speed %		
	Alt.(m)	Mach number			
1	10680	0.85	100	274.7	32361.93
2		0.7	100	242.5	27988.99
3		0.6	100	225.7	25737.17
4		0.5	100	212.1	23935.45

A computational simulation has been done for the flow upstream, around and through the intake in order to investigate the flow characteristics (i.e. pressure, temperature, velocity, density, Mach number etc…).

1st Case Sea Level; (M=0.02)

Figures 44 through 50 show Mach number, static to total pressure ratio, and static to total temperature ratio contours at sea level, 0.02 flight Mach number and mass flow rate of 679.45 kg/s.

Figure 44 shows that, the average Mach number increases in the axial direction towards the intake. At the fan inlet it has an average value of 0.45 (i.e. it behaves like a nozzle).

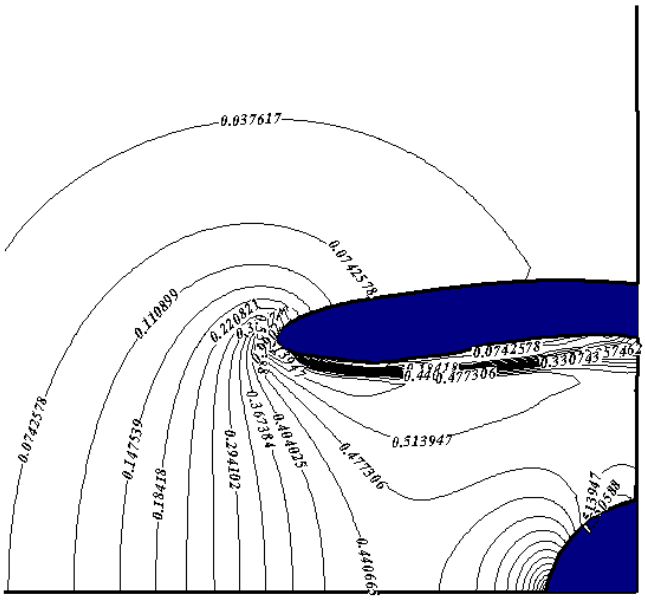

Figure 44: Mach number contours at sea level flight Mach number of 0.02 and mass flow parameter 0.1141.

Figures 45 and 46 illustrate the static to total pressure ratio and static to total temperature ratio contours, respectively. They show that the values of both static pressure and static temperature decrease in the axial direction towards the intake. They have an average value of (0.864 and 0.96) at the fan inlet.

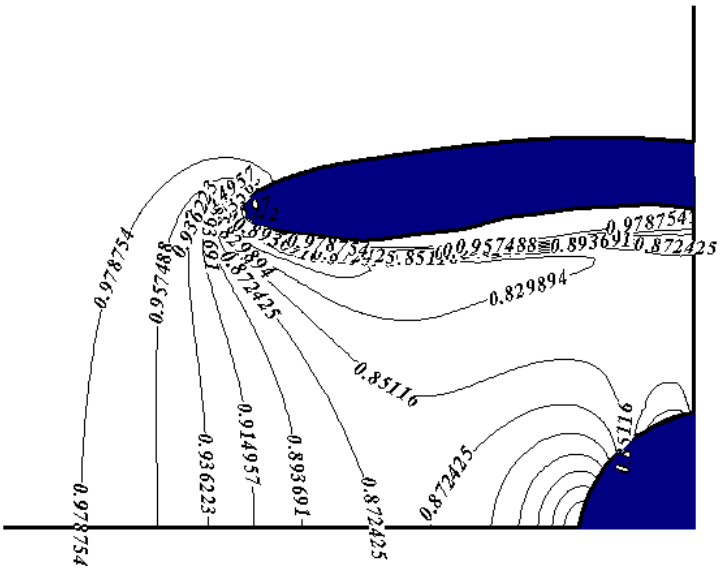

Figure 45: Static to total pressure ratio contours at sea level, 0.02 flight Mach number and mass flow parameter 0.1141.

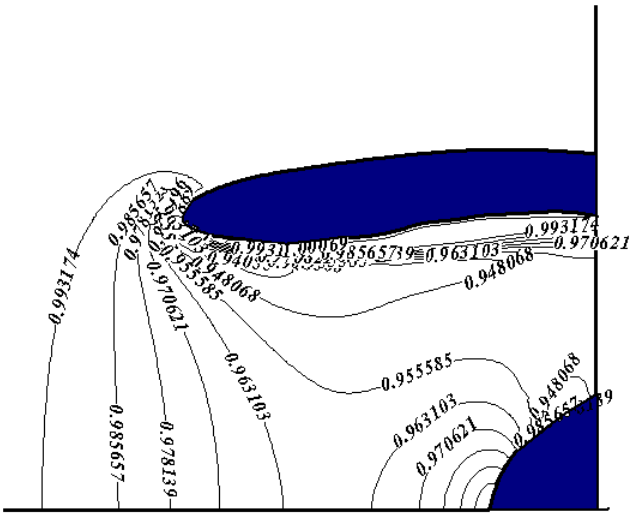

Figure 46: Static to total temperature ratio contours at sea level, 0.02 flight Mach number and mass flow parameter 0.1141.

Figure 47 (a), (b), (c) show the radial variations of the velocity magnitude at different axial locations (x=0.0, x=1.0 m, x=1.5m, from the intake lip). Figure (a) shows the radial variations of velocity magnitude at the intake lip. Figure (b) shows the radial variation of the velocity profile at an axial distance of 1.0 m from the intake lip, where a reverse flow is occurred due to the generated vortex at this location. Figure (c) shows the radial variation at the fan inlet which is at an axial distance of 1.5 m from the intake nose. Velocity changes from radius 1.2 m to radius 1.0 m and it has almost a constant value from radius 1.0 m to the fan boss surface.

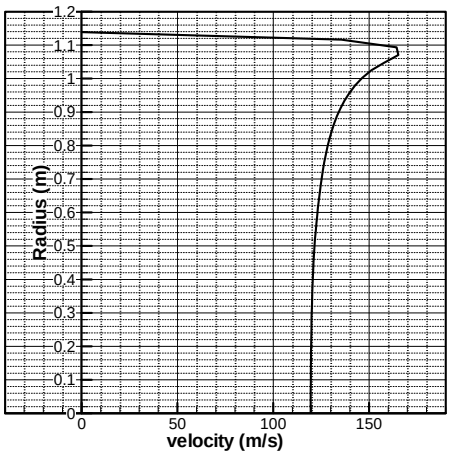

Figure 47a: Velocity distribution along radial direction at sea level and 0.02 Mach number at x=0.0 m.

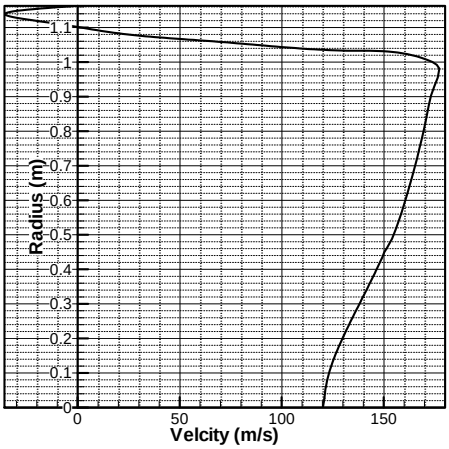

Figure 47 b: Velocity distribution along radial direction at sea level and 0.02 Mach number at x=0.5 m.

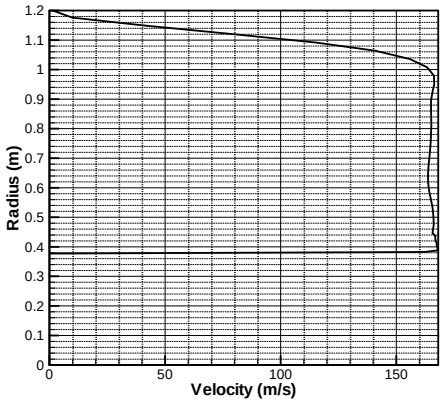

Figure 47c: Velocity distribution along radial direction at sea level and 0.02 Mach number at x=1.5 m.

Figure 48 shows that at centerline the Mach number increases in the axial direction towards and inside the intake until it reaches to its maximum value of 0.45 at 0.7 m, inside the intake and then it decreases until it reaches to zero at the nose of the boss. For 0.8 m, line the Mach number increases until the value of 0.52 at 0.7m, inside the intake, then it slightly decreases until it reaches 0.45 at the fan inlet.

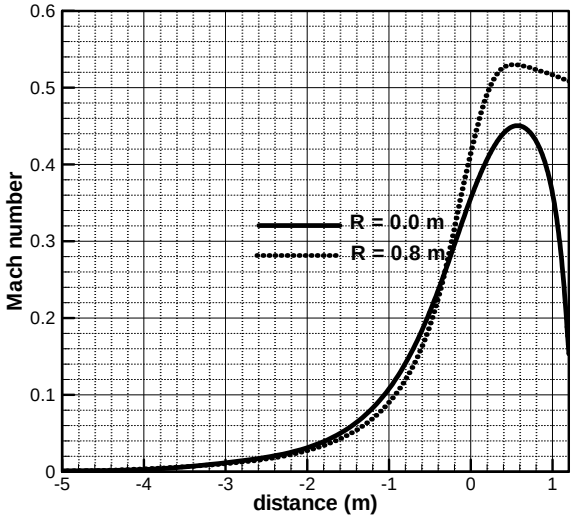

Figure 48: Mach number distribution along the axial direction at sea level, 0.02 Mach number and mass flow parameter 0.1141.

Figures 49 and 50 show the axial variations of static to total pressure ratio and static to total temperature ratio, respectively. At the intake centerline, both static to total pressure ratio and static to total temperature ratio are nearly constants from the far field to about 2 m, before the intake inlet, after that they start to decrease until they reach their minimum values (0.87, 0.97) at 0.7 m inside the intake, and then they increase until they take their stagnation condition at the boss nose. For 0.8 m, line the values of both static pressure and static temperature are constants from the far field to about 2 m, before the intake inlet; then they begin to decrease until they reach their minimum values (0.825, 0.945) at 0.7, m inside the intake. Finally they slightly increase to reach (0.86 and 0.95) at the fan inlet. In this case the intake acts like a nozzle until 0.7 m from the intake nose and then it behaves like a diffuser after that.

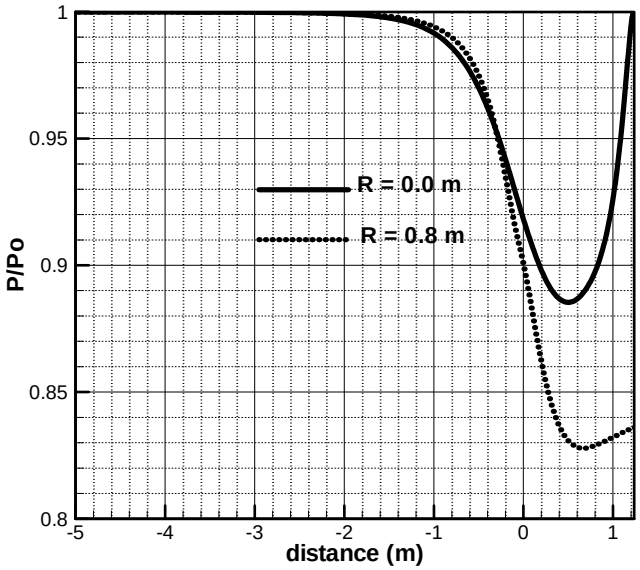

Figure 49: Static to total pressure ratio distribution along the axial direction at sea level, 0.02 Mach number and mass flow parameter 0.1141.

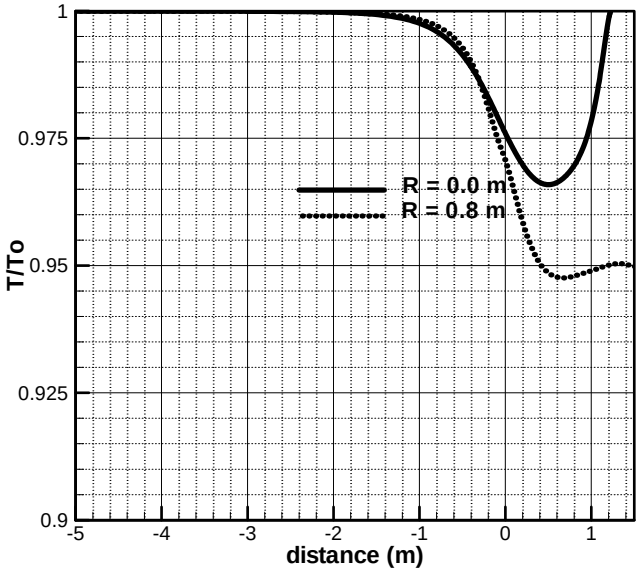

Figure 50: Static to total temperature ratio distribution along the axial direction at sea level, 0.02 Mach number and mass flow parameter 0.1141.

2nd Case (M= 0.6)

Figures 4.12 through 4.14 show the Mach number, static to total pressure ratio and static to total temperature ratio, contours respectively at flight Mach numbers 0.6 and altitude of 8461.5m.

Figure 51 shows the Mach number contours where the average value of Mach number at the intake inlet is 0.47.

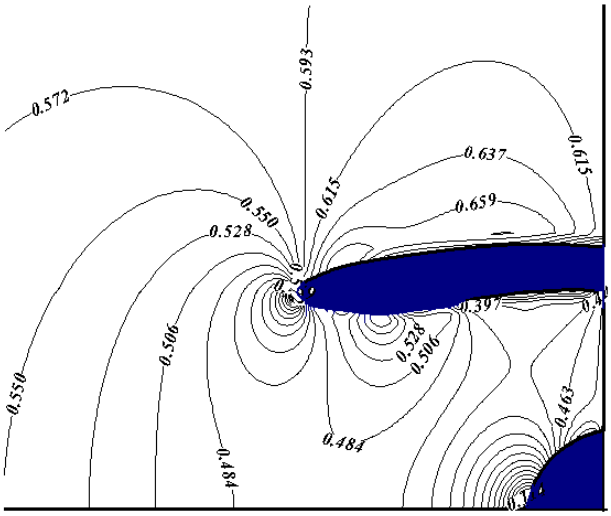

Figure 51: Mach number contours for flight Mach number 0.6 and mass flow parameter 0.1141.

Figure 52, 53 shows the contours of static to total pressure ratio and static to total temperature ratio for flight Mach number 0.6, where the average value of static to total pressure ratio and static to total temperature ratio at the fan inlet are (0.853, 0.95), while the average value of static pressure at the fan inlet is (0.866, 0.95).

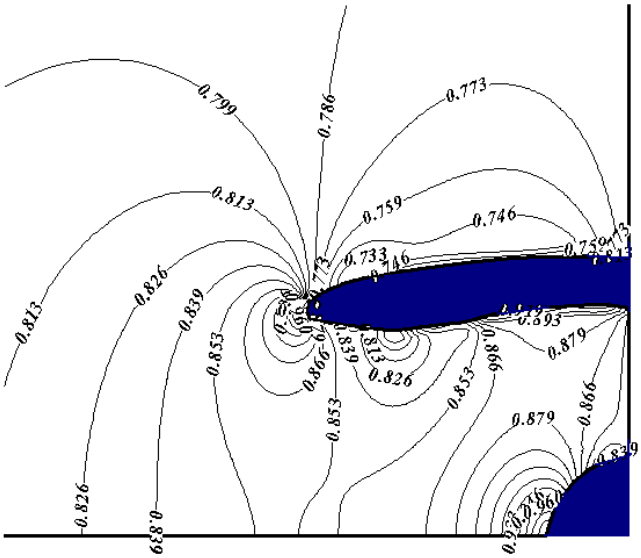

Figure 52: Static to total pressure ratio contours for flight Mach number 0.6 and mass flow parameter 0.1141.

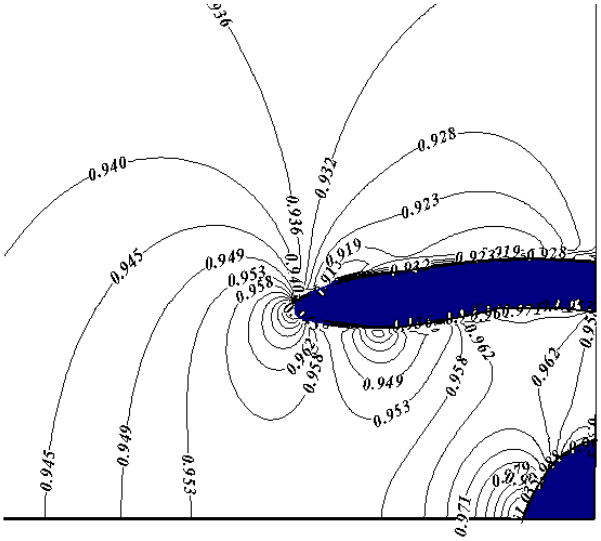

Figure 53: Static to total temperature ratio contours for flight Mach number 0.6 and mass flow parameter 0.1141.

Figure 54 shows that the Mach number at the centerline decreases along the intake axis until it reaches almost zero value at the fan nose. Along 0.8 m-line the Mach number decreases in the axial direction till the inlet of the intake where it takes a value about 0.45, and then it fluctuates around this value inside the intake.

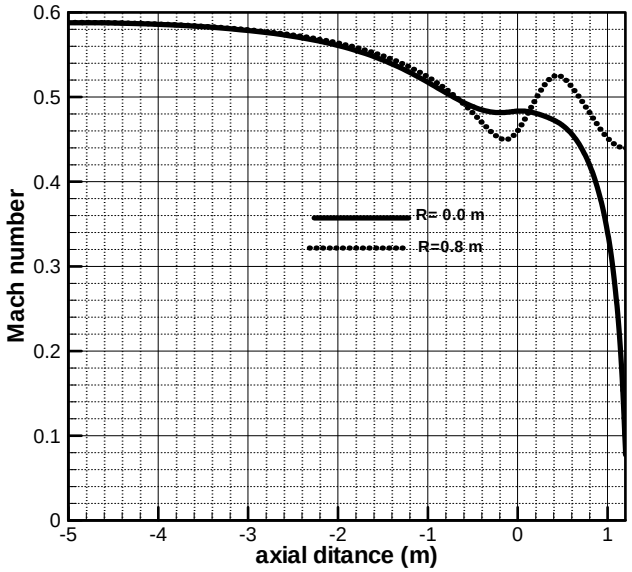

Figure 54: Mach number distribution along the axial direction for a flight Mach number 0.6 and mass flow parameter 0.1141.

Figures 55 and 56 illustrate that the values of static to total pressure ratio and static to total temperature ratio respectively, along the intake centerline their values increases towards the intake until they reach a stagnation values at the fan nose. Along 0.8 m-line the static pressure and static temperature increases in the axial direction till the inlet of the intake where they have a value of (0.86 and 0.96) at the fan inlet and they fluctuate around these same values.

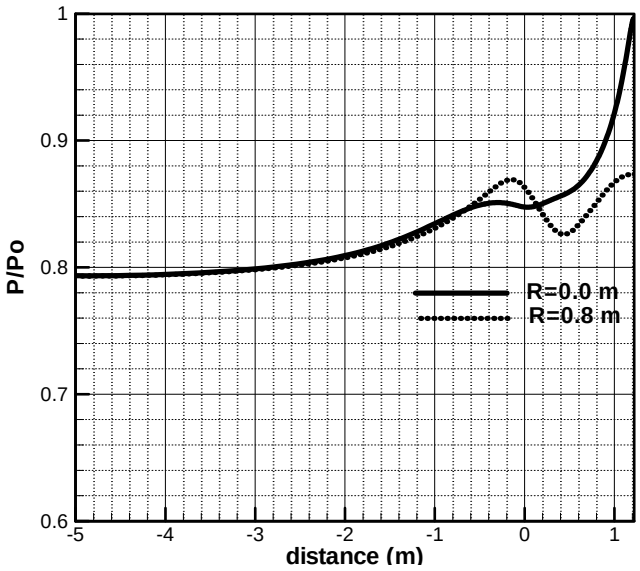

Figure 55: Static to total pressure ratio distribution along the axial direction for a flight Mach number 0.6 and mass flow parameter 0.1141.

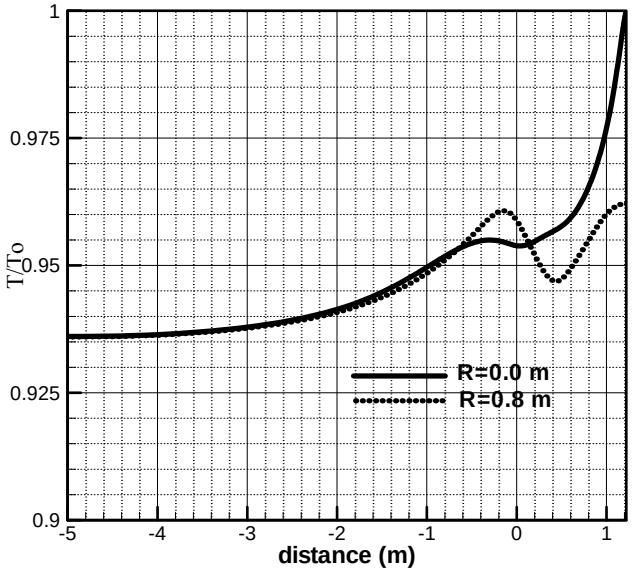

Figure 56: Static to total temperature ratio distribution along the axial direction for a flight Mach number 0.6 and mass flow parameter 0.1141.

3rd Case (M=0.85)

Figures 57 through 59 show the Mach number, static to total pressure ratio, static to total temperature ratio, contours, respectively at 0.85 flight Mach number and altitude of 8461.5m

Figure 57 shows the Mach number contours for flight Mach number 0.85. The average value of Mach number at the intake inlet is 0.47 and two supersonic bubbles are noticed at inlet lip and at a distance 1.28 m, along the outer surface.

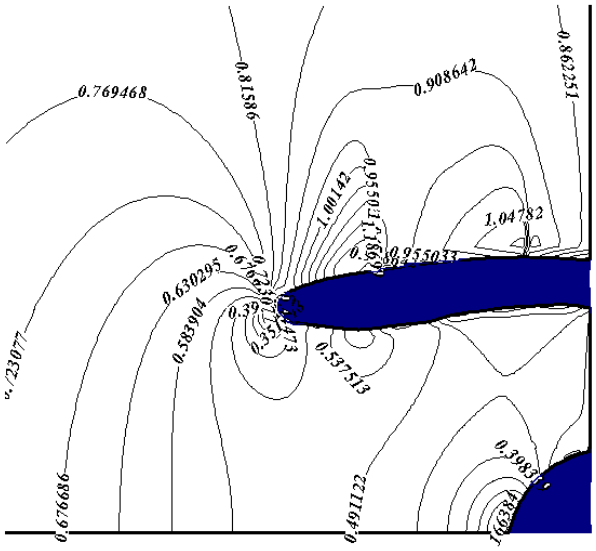

Figure 57: Mach number contours for a flight Mach number 0.85 and mass flow parameter 0.1141.

Figures 58 and 59 illustrate the static to total pressure ratio contours and the static to total temperature ratio contours, respectively. Both static to total pressure ratio, and static to total temperature, have an average value of (0.863 and 0.955) at the fan inlet. On the outer lip of the intake at an axial distance of 0.21 to a distance 0.49 m approximately from the intake nose the static to total pressure ratio and static to total temperature ratio have the minimum values, because of high Mach number at this location and again at a distance 1.28 m, along the outer surface due to supersonic bubbles.

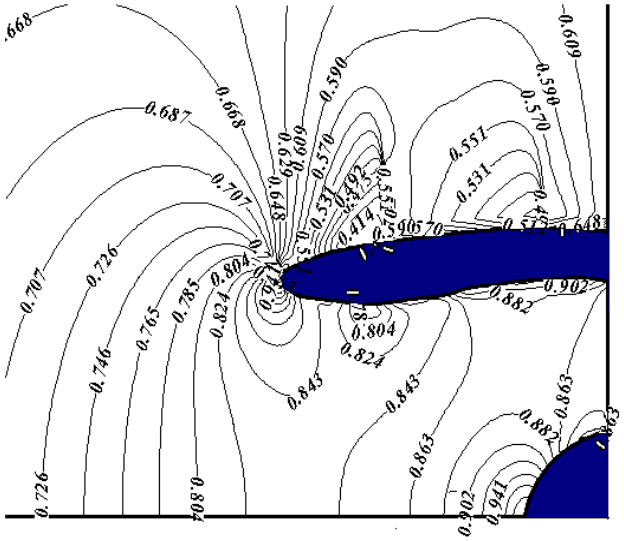

Figure 58: Static to total pressure ratio contours for flight Mach number 0.85 and mass flow parameter 0.1141.

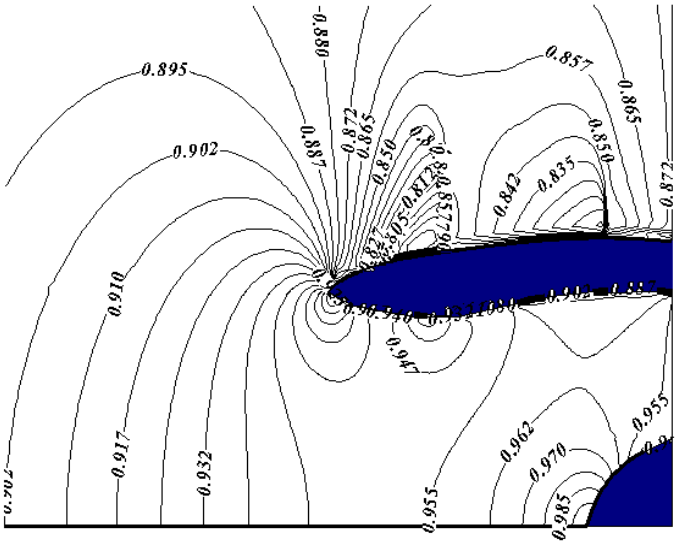

Figure 59: Static to total temperature ratio contours for flight Mach number 0.85 and mass flow parameter 0.1141.

Figure 60 shows that the Mach number at the centerline decreases along the intake axis until it reaches almost zero value at the nose of the boss. Along 0.8 m-line the Mach number decreases in the axial direction till the inlet of the intake where it takes a value about 0.45, and then it fluctuates around this value inside the intake.

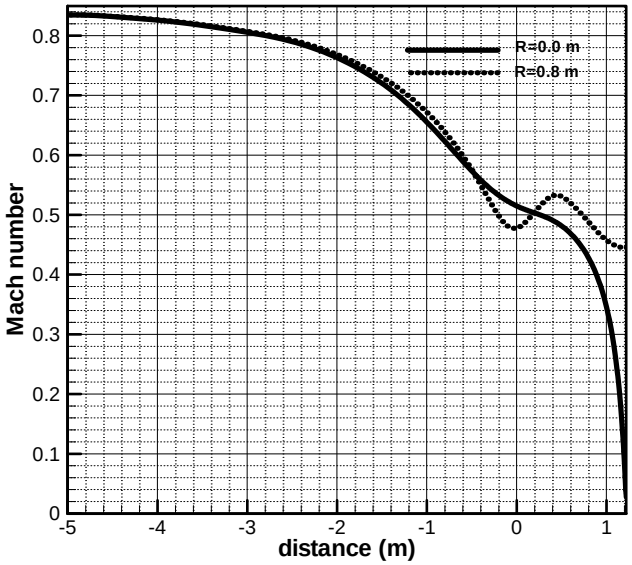

Figure 60: Mach number distribution along the axial direction for flight Mach number 0.85 and mass flow parameter 0.1141.

Figures 61 and 62 illustrate that the values of static to total pressure ratio and static to total temperature ratio, respectively, along the intake centerline their values increases towards the intake until they reach a stagnation values at the nose of the boss. Along 0.8 m-line the static pressure and static temperature increases in the axial direction till the inlet of the intake where they have a value of (0.865 and 0.956), and they fluctuate around these same values.

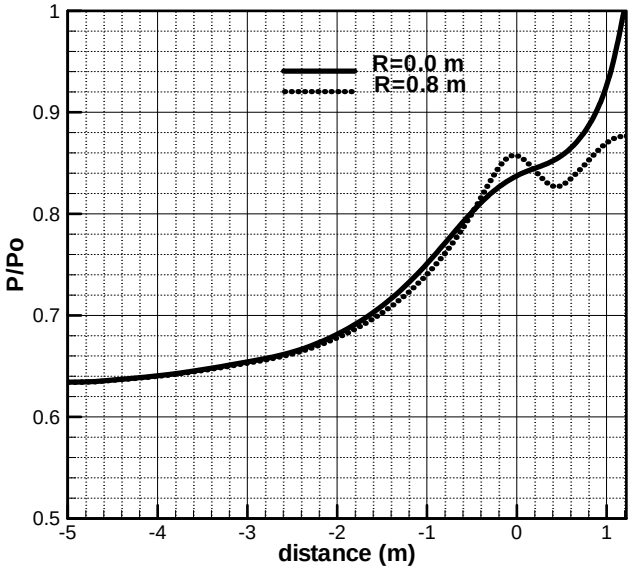

Figure 61: Static to total pressure ratio distribution along the axial direction for flight Mach number 0.85 and mass flow parameter 0.1141.

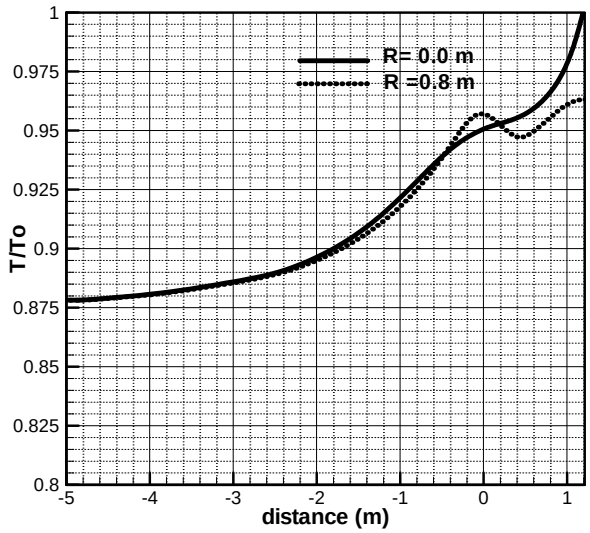

Figure 62: Static to total temperature distribution along the axial direction for a flight Mach number 0.85 and mass flow parameter 0.1141.

From this study we can conclude that: for certain corrected mass flow rate, the intake behaves like a diffuser or a nozzle according to the flight Mach number. For very low Mach number (0.0, 0.3 and 0.4) it acts as a nozzle for corrected mass flow rate of 0.1141. For other Mach number (0.6, 0.8 and 0.85) it acts like a diffuser for the same corrected mass flow rate. When the intake acts like a diffuser the compression occurs externally and when it acts as a nozzle the expansion occurs externally and internally. The distance through the intake where the internal expansion occurs depends on the flight Mach number.

Figure 63 gives the area ratio ($\frac{A_i}{A_\infty}$) variations against the flight Mach number for 0.1141 corrected mass flow rate. This confirms that the flow in a subsonic intake is a function of Mach number only and completely independent on the flight altitude.

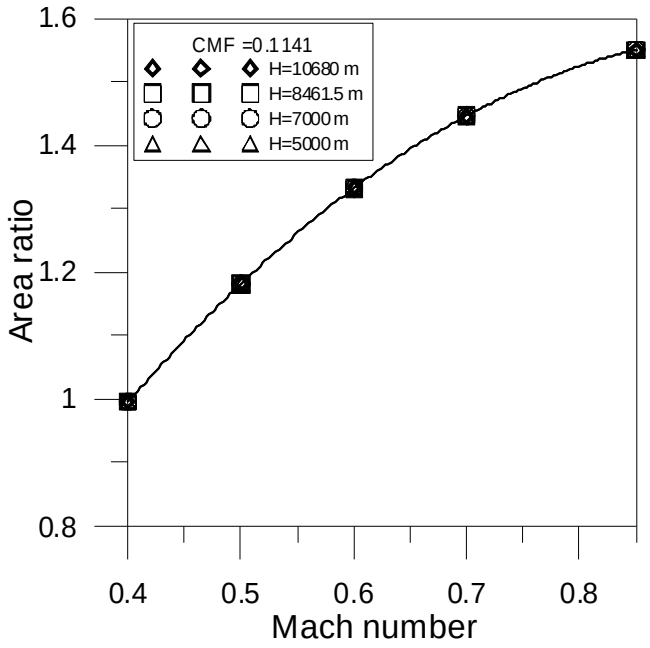

Figure 63: Area ratio variation versus flight Mach number for different flight altitudes and corrected mass flow rate 0.1141.

Figure 64 gives the area ratio ($\frac{A_i}{A_\infty}$) versus the flight Mach number for different corrected mass flow parameter. It shows that for certain flight Mach number as the corrected mass flow rate increases the area ratio decreases. At each mass flow parameter, there is a critical Mach number, which achieves an area ratio of unity.

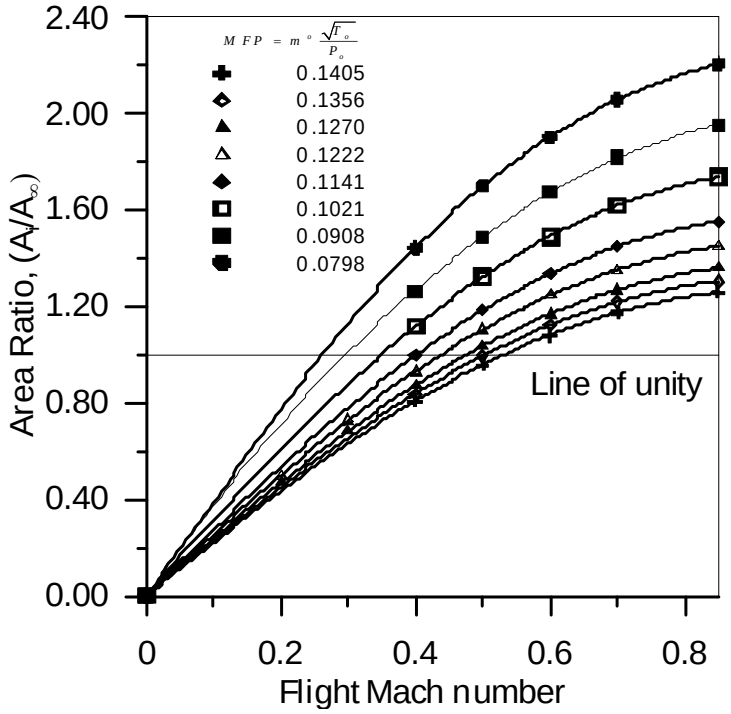

Figure 64: Area ratio variation versus flight Mach number for different corrected Mass flow rate.

Figure 65 shows the changes of the critical Mach number which is corresponding to unity area ratio versus the mass flow parameter.

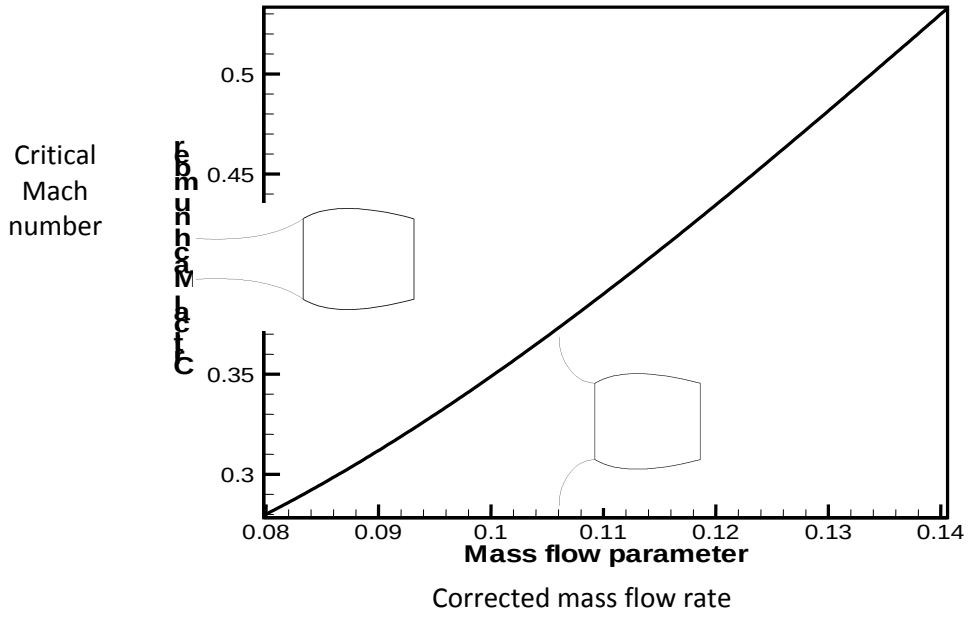

Figure 65: The critical Mach number corresponding to area ratio of unity versus corrected mass flow rate.

4.3 Droplets Trajectories and Ice Accretion

In-flight icing is a serious hazard. It destroys the smooth flow of air, increasing drag, degrading control authority and decreasing the ability of an airfoil to lift. Actually, the weight of the ice has a secondary effect relative to the airflow disruption, and the power is added in order to compensate the additional drag force and the angle of attack must be increased to compensate the lift force to maintain the same altitude. Unfortunately increasing the angle of attack increases the rate of accretion leading to a serious hazard or in the case of the aircraft engine the situation takes another aspects, the safety margin arises here as shown in figure 66 the intake shape changes due to ice accretion. "FLUENT" software [2] from "FLUENT.INC", is used for tracing water droplet trajectories to determine the impingements locations. After that, based on thermodynamic Messenger model, Hansman [3], a user defined function written in "C" is prepared and validated to determine the rate of ice accretions at each impingement, consequently the rate of ice accretion at each point on the intake. Finally a "FORTRAN" program is developed to calculate the ice thickness using the span-wise concept, which means that ice growth is perpendicular to the surface Bragg [4]. The new intake geometries are developed through the pre-processor "GAMBIT" to generate the new mesh for the new shape, and the flow is solved again to determine the flow properties changes.

Figure 66: Rime ice accretion on the intake of a small turbojet engine.

The new geometries represent a case file with the same boundary conditions and with the same mass flow rate through the intake. The droplets which impinge the intake surface given a boundary condition "Trapped", which means that this trajectory is terminated as the water droplet impinges that surface. When this condition occurs, the next step begins, which involves the computation of collection efficiency, and the fraction of impingement mass, and a heat balance process is performed to determine the frozen fraction. The icing problem is solved quasi-steady, where the total icing time is divided into a several number of steps. For each time step the trajectories, collection efficiency and the ice thickness are calculated. The geometry is updated and the flow is solved for a newer geometry. This routine is repeated for each time step until the total icing time is reached.

4.3.1 Droplet Trajectory Calculations

The clouds in the atmosphere contain supercooled water droplets of tiny sizes at low temperatures. These droplets have diameters of 10 to 50 microns, Hansman [3], Papadakis et al. [5] and experiences low Reynolds number enough to ensure that the droplets remain spherical in shape, Hansman [3]. The droplet trajectory can be developed either by Eulerian approach or by Lagrangian approach. In the Eulerian approach, droplets velocity is represented as average over the computational cell. The consideration of the droplet size distribution requires the solution of a set of basic equations for each size classes. The Eulerian approach is preferable for two-phase flows with uniform droplets size and volume fraction from 0 to 100 % and is applicable for evaporation, condensation, aeration problems. This means that no data will be available for the droplets track.

The Lagrangian approach model the droplets, droplets, bubbles dispersed (i.e. each droplet trajectory alone) for low volume fractions up to 10% of the continuous phase, by solving the equations of motion tacking into accounts the relevant forces acting on the droplets. The finite dimensions of the droplets are not considered and the flow around the individual droplets is not solved (i.e. the droplets is considered as point). The liquid water content at high altitudes has a value of 2 to 10 grams per cubic meters. Since we have a low volume water droplet fraction of the surrounding air, then Lagrangian approach is considered.

Trajectory Governing Equation

The droplets motion of a point mass supercooled water droplet in the flow domain is modeled by applying Newton's Second law, F=ma, to the droplet, this equation was developed by Soo, et al, stated by Bragg [4] as

$$m\left(\frac{d^2x}{dt^2}\right) = D + P + \overline{M_a} + B + mg \tag{4.7}$$

Where

$\overline{D}$: drag force on the water droplet

$\overline{P}$: Pressure gradient force

$\overline{M_a}$: Apparent mass force (virtual mass)

$\overline{B}$: Bassett force

$m\overline{g}$: Droplet weight term

These different types of forces are explained as follow

Drag Force

The steady state drag $\overline{D}$ is the drag force which acts on the droplets in a uniform pressure field when there is no acceleration or deceleration of the relative motion between the droplets and the continuous fluid. The drag force $\overline{D}$ at different Reynolds number is based on the drag coefficient C_D which is defined as:

$$c_D = \frac{\overline{D}}{0.5\,\rho\,\left(\overline{V} - \overline{V}_{drop}\right)^2\,a} \tag{4.8}$$

Where

a : cross sectional area of the spherical droplet

$\overline{V}$: fluid velocity

$\overline{V}_{drop}$: droplets velocity

The Reynolds number for a spherical droplet; $\mathrm{Re}_{droplet}$ is given by:

$$\mathrm{Re} = \frac{\rho\, d_{drop}\left|\overline{V} - \overline{V}_{drop}\right|}{\mu} \tag{4.9}$$

At very low relative velocities, Stokesian drag force is

$$\overline{D} = 3\,\pi\,\overline{\mu}\,d_{drop}\,\overline{V}_{drop} \tag{4.10}$$

Where

$\overline{\mu}$: is the viscosity of the fluid material,

d_{drop} : droplet diameter

$\overline{V}_{drop}$: droplet terminal velocity

Experiments yielded a so-called standard drag curve as shown in figure 67 for a single solid sphere moving at a constant velocity in isothermal, incompressible, still air.

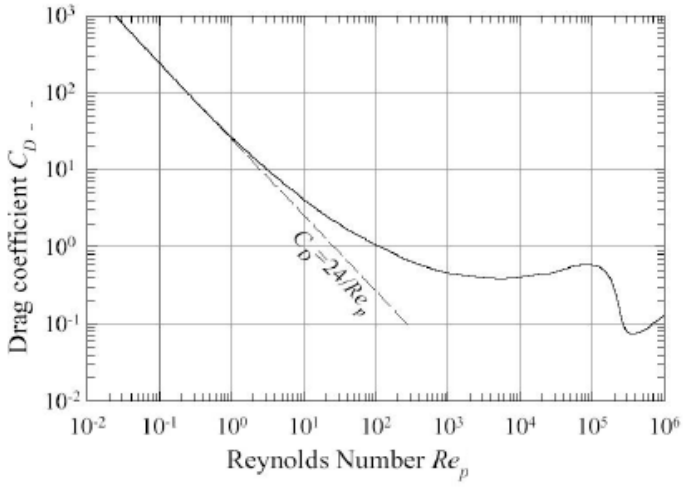

Figure 67: Variation of Drag force coefficient C_D with Reynolds number.

Dynamic Drag Model

Many droplet drag models assume the droplet remains spherical throughout the domain.

The drag of a spherical object at different Reynolds numbers is determined by the following

$$C_{D,sphere} = \begin{cases} 0.424 & Re > 1000 \\ \dfrac{24}{Re_{drop}}\left(1 + \dfrac{1}{6}\,Re^{\frac{2}{3}}\right) & Re < 1000 \end{cases} \tag{4.11}$$

However, as an initially spherical droplet moves through a gas, its shape is distorted significantly when the Weber number is large. In the extreme case, the droplet shape will approach that of a disk. The drag of a disk, however, is significantly higher than that of a sphere. Since the droplet drag coefficient is highly dependent upon the droplet shape, a drag model that assumes the droplet is spherical is unsatisfactory. The dynamic drag model accounts for the effects of droplet distortion, linearly varying the drag between that of a sphere, Equation (4.11) and a value of 1.54 corresponding to a disk [2]. The drag coefficient is given by

$$C_D = C_{D,sphere}\,(1 + 2.632\,y) \tag{4.12}$$

Where

y: is the droplet distortion, as determined by the solution of

$$\frac{d^2y}{dt^2} = \frac{C_F \rho_{air} u^2}{C_b \rho_w r^2} - \frac{C_k \sigma}{\rho_w r^3} y - \frac{C_d \mu_w}{\rho_w r^2} \frac{dy}{dt} \tag{4.13}$$

Where

ρ_w : is the droplet density

ρ_a : is the air density

u: is the relative velocity of the droplet

r: is the undisturbed droplet radius

σ : is the droplet surface tension

μ_w : is the droplet viscosity

and the constants are $C_k = 8$, $C_d = 5$ $C_F = 1/3$, and C_b is a constant equal to 0.5 if break-up is assumed to occur when the distortion is equal to the droplet radius, i.e., the north and south poles of the droplet meet at the droplet center. In the limit of no distortion (y = 0), the drag coefficient of a sphere will be obtained, while at maximum distortion (y = 1) the drag coefficient corresponding to a disk will be obtained.

Pressure Gradient Force

The pressure force is due to local pressure gradient in the flow which gives an additional force in the direction of the pressure gradient. A combination of the pressure gradient with the shear stress produces an expression that is a function of the ratio of the flow density to the droplets density. It can be neglected for the case of gas solid flow because of its small value, Sommerfeld [2]. This force which is determined according to the following equation,

$$\overline{P}_i = \left(\frac{\rho}{\rho_w}\right) u_{i,w} \frac{\partial u_j}{\partial x_i} \tag{4.14}$$

Virtual Mass Force

The virtual mass force is due to the acceleration or the deceleration of droplets in the fluid flow. This force can be neglected for the case of dilute gas solid flow. This force can be written as

$$\overline{M}_a = \frac{1}{2} \frac{\rho}{\rho_w} \frac{d}{dt} \left(u_i - u_{i,p}\right) \tag{4.15}$$

and is important when.

$$\rho_{air} << \rho_w$$

For a water droplet moving in air the density of the droplets is much greater than that of air, the pressure gradient term and the apparent mass term is may be neglected, Bragg [4]. The Bassett force term accounts for the deviation of the flow pattern around the droplet which represents the history of motion on the

instantaneous force. This force term is significant if the droplet density is of the same order as that of the fluid, or if the droplet experiences large acceleration.

Bragg [4] has shown also that for the icing process the acceleration experienced by the droplets are not large enough foe Bassett force term to be significant. Lee, et al. [6] showed that the effect of gravity force can be negligible by conducting a semi-empirical model and added it to the LEWICW software. Therefore the equation (4.7) can be written using the previous assumptions as

$$m\left(\frac{d^2x}{dt^2}\right) = D \tag{4.16}$$

4.3.2 Ice Accretion Mechanism

The ice accretion process is controlled physically by two distinct sub-processes. The first is the inertial transport of liquid water droplets from the ambient environment to the engine inlet surface. Once the droplets have impinged the surface, their freezing becomes controlled by thermodynamic process. If the heat transfer from the surface is sufficient to remove all the latent heat of freezing of the impinging water droplets, the water droplets freezes rapidly on impact and resulting in a dry ice surface called “rime ice”, its shape protrudes forward into the air-stream; figure 68. When the heat transfer from the surface is inadequate to remove all of the latent heat transfer from the impinging droplets, the ice surface becomes wet, which characterized as glaze ice. In this situation a fraction of the incoming droplets freezes on impact and the remainder run back in the flow direction due to the shear stress of the air flow on the aircraft surface, while the heat transfer process is continuously occurred. This behavior of the droplets after impingement process produces an irregular ice shape, which changes the aerodynamic properties of the exposed surface. There are many factors affect the ice accretion process, such as liquid water content (LWC), droplets size, ambient temperature, and air flow velocity.

Rime Glaze

Figure 68: Icing patterns.

Liquid Water Content

Liquid water content (LWC) influences the severity of the ice accretion process in two ways. First, increasing LWC implies larger accretions within a given time interval. Thus high LWC implies a greater severity of the icing encounters. The second effect of high LWC is to cause the ice accretion to transition from rime to mixed icing due to the higher impinging water load on the icing surface; figure 69.

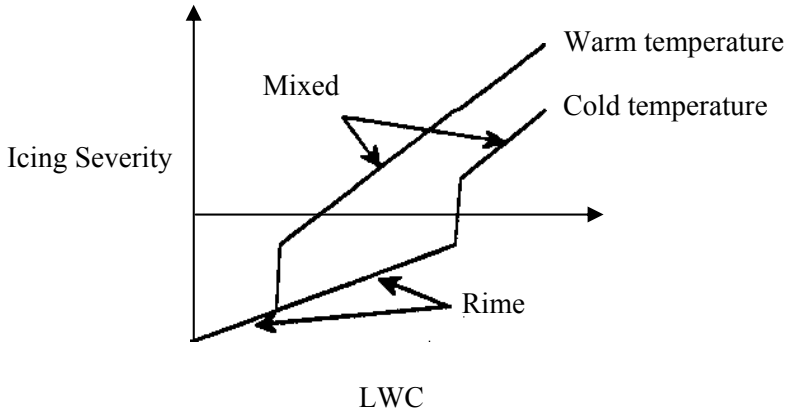

Figure 69: The relation between LWC, Temperature and icing severity, Hansman [3].

Droplet Size

The size of the ambient water droplets both in terms of the median volumetric diameter (MVD), which is defined by equation (4.17) and the actual shape of droplet size distribution can be important to the ice accretion process. As the droplet size increases the more the efficiently caught by the body; figure 70. These effects have been quantified for typical cloud and rain size distribution by Hasnman [3].

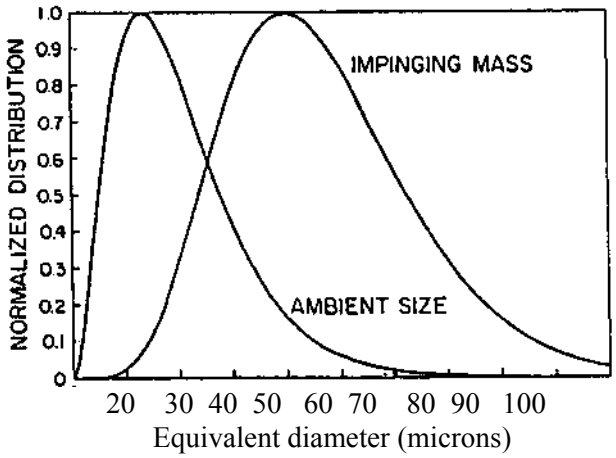

Figure 70: Khrigian-Mazan ambient cloud droplet size distribution and resulting impinging mass flux distribution, Hasnman [3].

Figure 70 shows the impinging mass distribution function and the ambient size distribution function for a Khrigian-Mazan, Hasnman [3] distribution with 20 μm mean effective droplet diameter.

$$MVD = \sum_{i=1}^{N} D_i F_v(D_i) \tag{4.17}$$

It can be seen that the bulk of the impinging mass results from the small number of the large droplets in the tail of distribution. The (MVD) and the shape of the distribution therefore determine the effective collection efficiency of the exposed surface.

Temperature

The non linear dependence of icing severity on total air temperature (TAT) combined with aircraft velocity effects makes it difficult to accurately identify regions of moderate or severe ice potential from ambient air temperature alone.

Air Flow Velocity

The aircraft velocity or (air flow velocity) affects the collection efficiency of liquid water and the thermodynamics of the icing process. Increasing velocity results in higher impinging liquid water exposure by increasing both the path swept out by the aircraft trajectory in a given time and the collection efficiency surfaces. Thermodynamically, the velocity affects the heat transfer and (LWC) load through the increased impinging water mass and through increasing the stagnation point temperature at high velocities.

Collection Efficiency

The local collection efficiency is an internally determined quantity which involves the individual droplet trajectories as they pass through the flow field surrounding the intake. Because it's sensitive to the details of the flow field and may be influenced by a variety of parameters, the local collection efficiency is normally evaluated by a droplet trajectory analysis around the intake and the local collection efficiency is defined from the following relation

$$\beta = \frac{\text{locally impinging droplet flux}}{\text{free stream droplet flux}}$$

$$\beta \leq 1.0$$

Where

β : collection efficiency

The collection efficiency "impingement efficiency" is a dimensionless parameter, which is defined as the ratio of the impinging mass at certain incremental area on the intake surface with respect to the far field mass flux enclosed in the two impinging trajectories that bounded this area.

Based on the aforementioned definition of the local collection efficiency there are two methods can utilized to calculate the collection efficiency. The first method considers the impinging mass flux as expressed by the arc length. ΔS along the intake surface, while the far field mass flux is expressed by the distance Δy as shown in

figure 71. If the there are two adjacent droplets trajectories having a vertical distance δy from each other and impinges the surface of the intake over a length δS hence the collection efficiency is calculated by tacking the limit as the following,

$$\beta = \lim_{\delta s \to 0} \frac{\delta y}{\delta s} \tag{4.18}$$

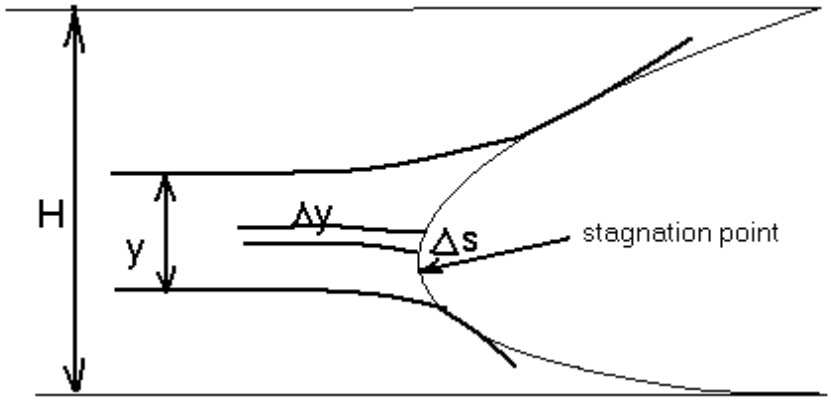

Figure 71: The collection efficiency in terms of the ratio between distances of two adjacent streamlines at the far field and points of impact respectively [7].

In the second method, the cosine of the angle between the trajectory slope at point of impingement and the normal to the surface (ϕ) at same point; figure 72, gives the locally collection efficiency as the following equation,

$$\beta = \cos(\phi) \tag{4.19}$$

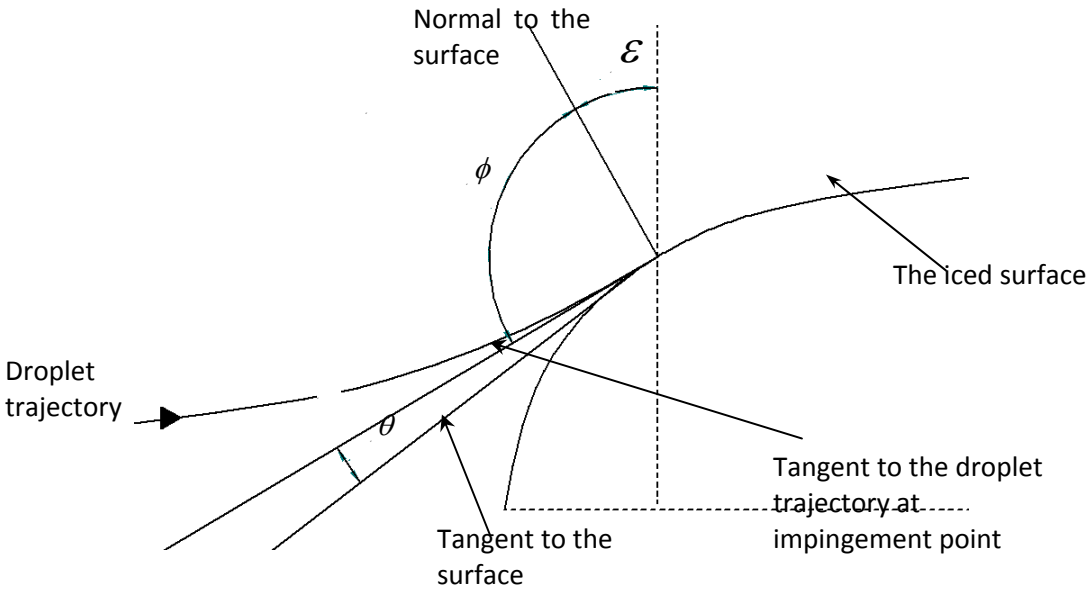

Figure 72: The collection efficiency in terms of tangent to the stream line and the normal to the surface at point of impact, Bragg [4].

This method is a more applicable than the previous one because the droplet velocity value and direction can be read by the user defined function just before the collision occur, also the area increment direction where the collision takes place is read by the user defined function. Consequently the angle between the tangent to the droplet trajectory and the normal to the wall at point of impingement (ϕ) can be known the so the collection efficiency.

Steady State Thermodynamic Model for an Icing Surface

The thermodynamic analysis presented her is based on the earlier work by Hansman [3] and is commonly employed in current ice accretion models. Figure 73 shows the principle modes of energy transfer associated with an icing surface.

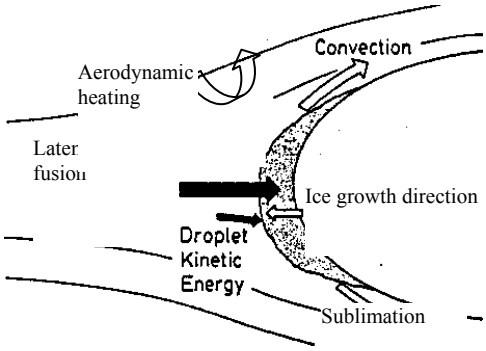

Figure 73: Modes of energy transfer for accreting ice surface, Hansman [3].

Heat is added to the surface primarily not only from the latent heat of fusion released as the droplets freeze, but also from aerodynamic heating and, an even smaller extent, from the kinetic energy of the droplets impacting the surface. Heat is removed from the surface primarily by convection, and to a lesser degree by sublimation (when the surface is dry) or evaporation (when the surface is wet). In addition, heat is absorbed from the surface as the supercooled droplets impinge the surface.

It is assumed that the only liquid entering the control volume is due to the impinging droplets. A heat balance process is performed to calculate the quantity of the freezing mass, so a freezing fraction is calculated from the following equation

$$n = \dot{Q}_{out} / [\dot{Q}_{in}] \quad (4.20)$$

where $\dot{Q}_{in}''$ and $\dot{Q}_{out}''$ represents the rate of energy added to and removed from, respectively, from the control volume per unit area per unit time. If the ice surface is wet, this mean that insufficient heat is being removed to freeze all of the impinging liquid, and therefore the "freezing fraction" n is less than unity.

The double prime superscript is used to indicate that the quantity is defined per unit area of the icing surface. When the ice surface is dry the freezing fraction is equal to unity or greater than unity, where the ice formed is a rime ice. This means that the heat removed from the control volume is equal to or higher than that added to the control volume and when the frozen fraction is less than unity part of the impingement droplet mass is frozen and the other is run back under the shear stress forming glaze ice. In steady state the rate at which energy is added to the control volume and the rate at which it is removed are constant as the following,

$$[\dot{Q}''_{out}] = constant \quad (4.21)$$

The rate of heat added is expanded into the following,

$$[\dot{Q}''_{in}] = [\dot{Q}'']_{freezing} + [\dot{Q}'']_{(aero\ heating)} + [\dot{Q}'']_{(drops\ kinetic\ energy)} \quad (4.22)$$

Where

$\dot{Q}''_{in}$: is the input heat flux to the control volume

$\dot{Q}''_{freezing}$: is the heat flux required to freeze a certain mass

$\dot{Q}''_{aero\ heating}$: is the kinetic heat flux of air

$\dot{Q}''_{drops\ \text{kinetic energy}}$: is the droplet kinetic energy

Each of the above terms are computed from the following equations

$$\dot{Q}''_{freezing} = \dot{M}''\left[L_f + C_i\left(T_{freezing} - T_{surface}\right)\right] \tag{4.23}$$

Where

$\dot{M}''$: is the mass flux of the impinging water droplets

L_f : is the latent heat of solidification

C_i : is the specific heat of ice

$T_{surface}$: is the uniform equilibrium surface temperature

$T_{freezing}$: is the water freezing temperature at certain altitude

$$\left[\dot{Q}''\right]_{(aero\ heating)} = (r\ h\ \left[U_\infty\right]^2)/\left[2\ C\right]_p \tag{4.24}$$

Where

r: recovery factor , 0.875

h: local convective heat transfer coefficient

U_∞ : the free stream velocity

C_p : constant pressure specific heat

The local convective heat transfer coefficient is known after the air flow, where the energy equation is applied, solution is converged. As mentioned previously the nacelle and hub are given a constant surface temperature, and hence from the solution of the energy equation the heat flux is determined. When applying

Newton's cooling law the convective heat transfer can be calculated and accessed by the user defined function to calculate the frozen fraction.

$$\frac{\dot{Q}_{drops\ kinetic\ energy} = \dot{M}'' U_{\infty}^{2}}{2} \tag{4.25}$$

Where

$\dot{M}''$: is the mass flux of the impinging water droplets

Also the rate of the heat removed is expanded as the following,

$$\dot{Q}_{out}'' = \dot{Q}_{convection}'' + \dot{Q}_{sublimation/evaporation}'' + \dot{Q}_{drops\ warming}'' \tag{4.26}$$

Where

$\dot{Q}_{out}''$: is the output heat flux from the control volume

$\dot{Q}_{conv.}''$: is the convective heat flux from the control volume

$\dot{Q}_{sublimation/evaporation}$: is the sublimation or evaporation heat flux from the control volume

$\dot{Q}_{drops\ warming}''$: is the droplet warming heat flux from the control volume

Each constitute of the above terms are computed from the following relations

$$\dot{Q}_{convection}'' = h(T_{surface} - T_{\infty}) \tag{4.27}$$

Where

T_{∞}: is the cloud temperature

$$\dot{Q}_{sublimation/evaporation}'' = (hDL_{s/v})/k\ (\rho_{v,surf.} - \rho_{v,\infty}) \tag{4.28}$$

Where

D: diffusion coefficient of water vapor in air

$L_{s/v}$: is the latent heat of sublimation or vaporization

$\rho_{v,surf}$: is the saturated vapor density over the surface

$\rho_{v,\infty}$: is the saturated vapor density in cloud

In the iced layer there is no temperature gradient is assumed, consequently the third term is dropped and there is no conduction take place in the ice layer

The total mass flux, $M^{"}$, of droplets impinging on a body in the above equations can be written as

$$M^{"} = \beta W U_{\infty} \tag{4.29}$$

Where W is the cloud liquid water content.

Ice Thickness Calculation

The ice accretion on the intake is happened from the water droplets which impinges the exposed surface, and accumulates on it. This accumulation process causes the surface shape to changes. The new dimensions of the intake are calculated after adding the volume of the ice accreted. Figure 74 shows the ice growth (cross hatched) on a small segment of a curved surface (ds), where φ is the assumed direction of ice growth and r is radius of curvature of the surface.

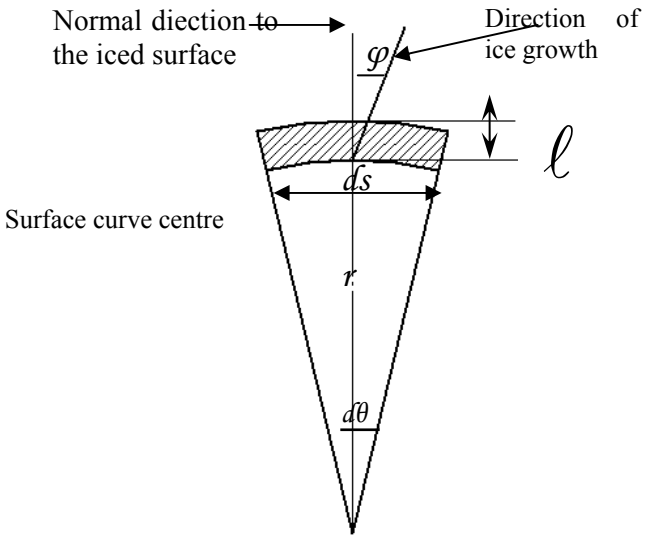

Figure 74: Geometry of ice growth calculation, Bragg [4].

Bragg [4] developed an equation for ice thickness calculation from the geometry

$$l + \frac{l^2}{2r} = \frac{\dot{M}^{"}\beta}{\rho_{ice}\cos\varphi} \tag{4.30}$$

Where

ℓ : ice thickness

ρ_{ice} : ice density

φ : growth direction

In the first run, allow the ice to grow out normal to the surface. Herein the value of φ equals zero, and the above equation can be rewritten in the following form

$$l + \frac{l^2}{2r} = \frac{\dot{M}^{"}\beta}{\rho_{ice}} \tag{4.31}$$

Herein a non-linear term arises due to the radius of curvature, r. The non linear term can be neglected for large radius of curvature or large leading edge, which our case, or for small values of (*l)* which can be achieved by taking a small time steps. Then the ice thickness can be calculated from the following equation

$$l = (\dot{M}^{"} \beta)/\rho_{ice} \tag{4.32}$$

General computational procedure

The ice accumulation on the intake surface leads to its geometry change with time. Since the ice accretion phenomena depends on the geometry of the intake shape, thus during the simulation process the intake geometry must be updated for each time step. So the icing problem is considered to be quasi-steady.

For each time step the following procedure is carried out:

a) Flow field is solved

b) Droplets trajectories are calculated

c) Ice shape is defined

d) Intake geometry is updated and the new mesh is generated

These procedures are repeated for several time steps until the total icing time is reached

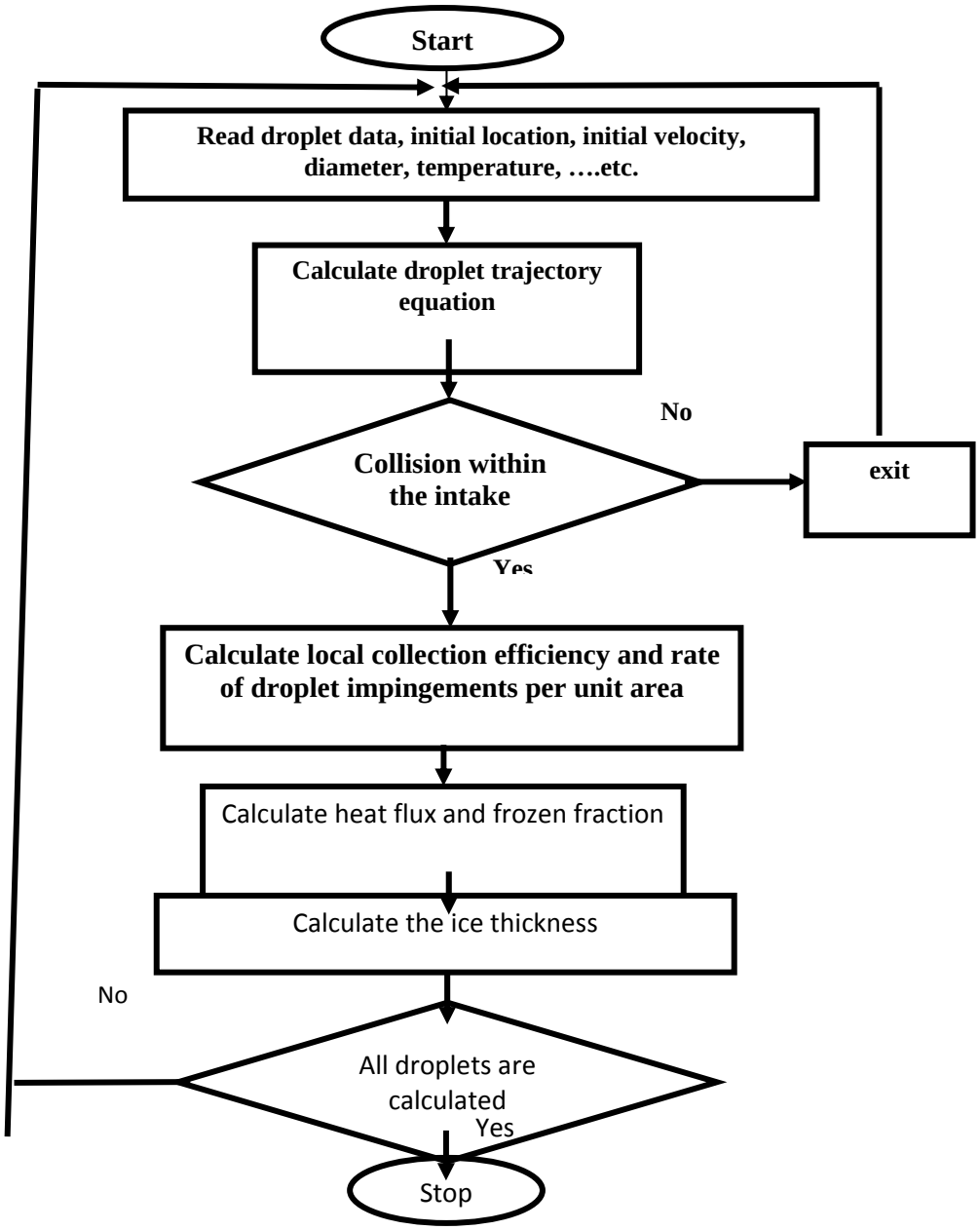

Figure 75: The general procedure of the ice accretion prediction.

4.3.3 Results and Discussion

As mentioned before the ice accretion problem is considered to be a quasi-steady one, within certain time steps. The smaller the time step means the more accurate solution of the problem. Herein the effect of the time step is studied and the solution is carried out. The solution is examined for three values of time steps, one minute, and two and half minute (2.5) and 5 minute. Figure 76 shows the ice accretion for those time steps at

20 m minute. It obvious that two and half time steps is approximately the same like the results for one minute time steps but for the case of five minute time steps there are an evident difference which is explained as the cumulative error of the solution. Fortunately, for these values of time steps there are no significance effect on the results of gas flow, consequently the five minute time step is chosen.

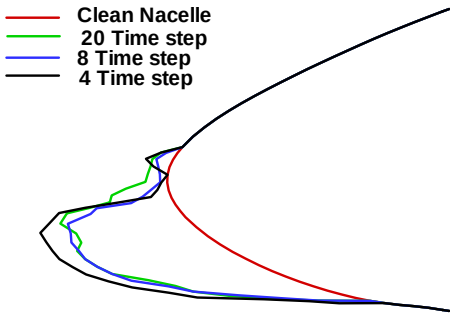

Figure 76: Effect of time step on ice accretion for flight altitude 8461 m, Mach number 0.8, and LWC 10 gm/m^3 at 20 min.

Figures 77 through 89 give the icing characteristics, such as the envelop of the impinging droplets trajectories, the ice accretion and the local collection efficiency at 8461.5 m altitude and 10 gm/m^3 LWC for different water droplet diameters (15,25,35,50 microns) and Mach number (0.8, 0.6, 0.4, 0.3).

Figure 77 shows the icing characteristics for 0.8 flight Mach number and different droplet diameter (15microns). Figure 77 (a), (b), (c) shows the envelope trajectories, the ice growth with time and the local collection efficiency at a droplet diameter of 15, microns. The envelope trajectories shows that the impingements locations are in the inside portion of the intake and this can be concluded also from the plot of the local collection efficiency. In the figure of the local collection efficiency, the plot starts at zero which represent the intake nose, and propagates with the positive values which is the inside portion of the intake surface and finally finishes at 0.117 m. In addition the ice growth is taken place on the inside portion of the intake while the ice growth on the boss of the fan is approximately axi-symmetrical because of the symmetric distribution of air velocity around the boss.

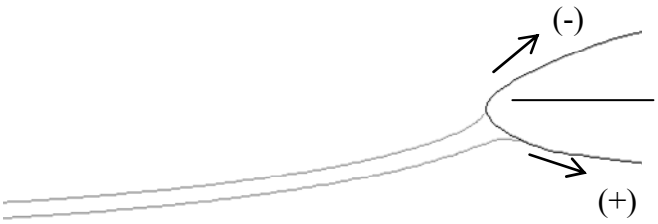

(a). The upper and lower envelop of the droplet trajectories.

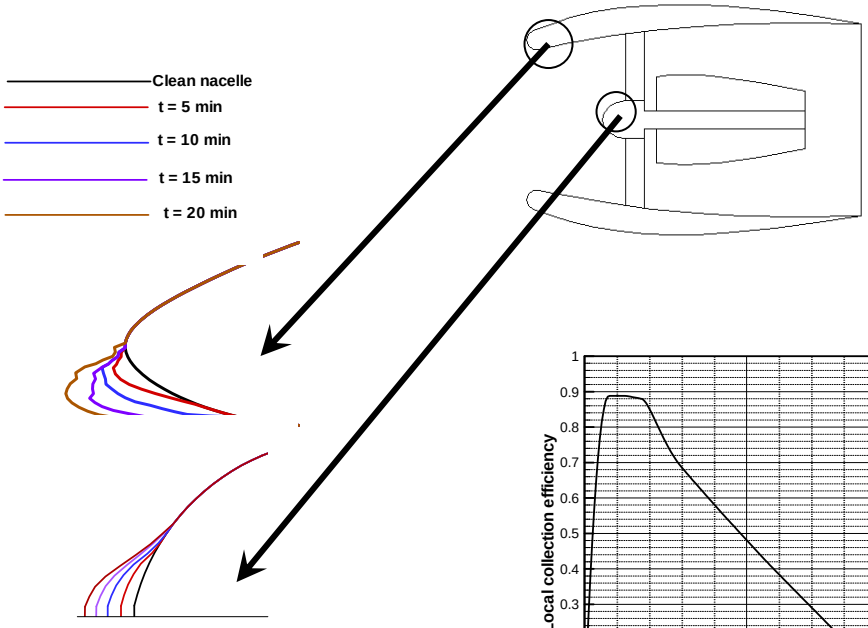

(b). The ice growth.

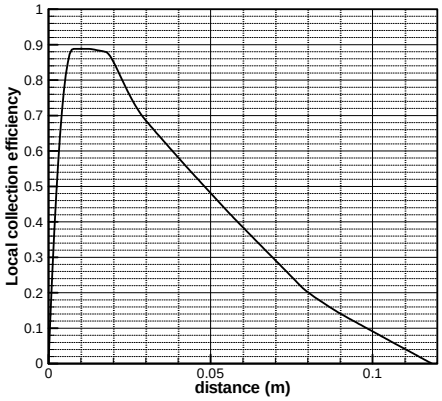

(c). The local collection efficiency for the clean nacelle.

Figure 77: Ice accretion (altitude 8461 m, M= 0.8, 15 micron diameter and 10 gm/m^3 LWC).

Figure 78 (a), (b), (c) shows the envelope trajectories, the ice growth with time and the local collection efficiency at a droplet of diameter 50, microns. The envelope trajectories show that most of the impingements locations are in the inside portion of the intake and some of it is above the nose and this can be concluded also from the plot of the local collection efficiency. In the figure of the local collection efficiency the plot starts at -0.05 approximately and propagates with the positive values which is the inside portion of the intake surface and finally finishes at 0.28 m. In addition most of the ice growth is taken place on the inside portion of the intake while the ice growth on the fan nose is approximately axi-symmetrical because of the symmetric distribution of air velocity around it.

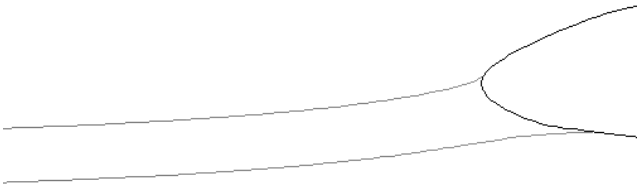

(a). The upper and lower envelop of the droplet trajectories.

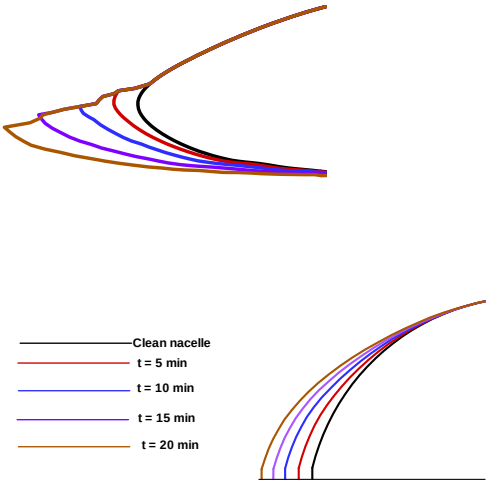

(b). The ice growth

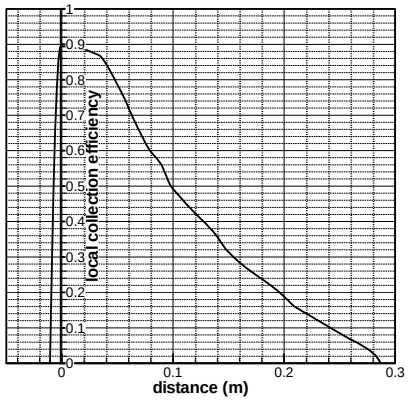

(c). The local collection efficiency
for the clean nacelle.

Figure 78: Ice accretion variables at altitude 8461 m, flight Mach number 0.8, 50 micron droplet diameter and 10 gm/m^3 LWC.

From both figures it could be concluded that as the droplet diameter increases the rate of the ice accretion increases and the ice propagates more on the inside surface of the intake and a little ice growth has been occurred above the nose of the intake because of the separation of the gas flow in this region which causes the droplet trajectories to deviate away from the intake surface, also for the above cases the values of the maximum local collection efficiency has a fixed value of 0.9 and its location is shifted towards the outer surface of the intake as the droplet size increases.

Figure 79 (a), (b), (c) shows the envelope trajectories, the ice growth with time and the local collection efficiency at a droplet diameter of 25, microns. The envelope trajectories show that most of the impingements locations are in the inside portion of the intake and some of it is above the nose but the outside subjected area is larger than the corresponding case for 0.8 flight Mach number and this can be concluded also from the plot of the local collection efficiency. In the figure of the local collection efficiency the plot starts at -0.02 approximately and propagates with the positive values which is the inside portion of the intake surface and finally finishes at 0.105 m. In addition most of the ice growth is taken place on the inside portion of the intake while the ice growth on the nose of the fan is approximately axi-symmetrical due to air flow symmetry.

(a). The upper and lower envelop of the droplet trajectories.

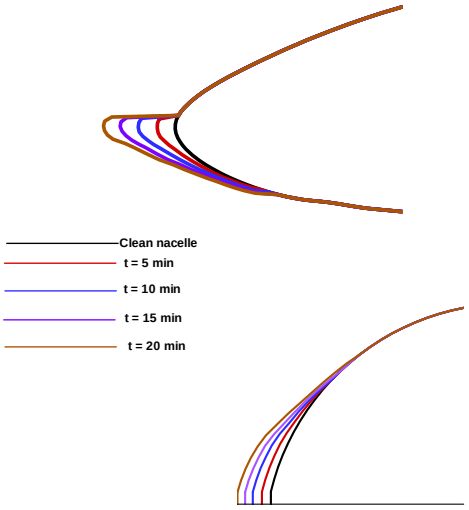

(b). The ice growth

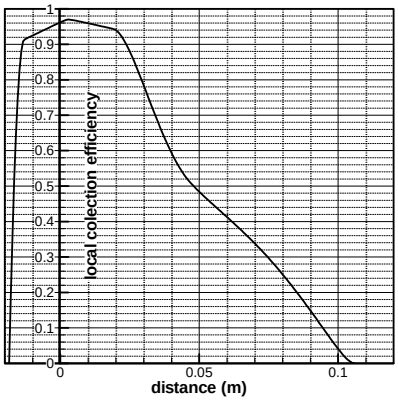

(c). The local collection efficiency for the clean nacelle.

Figure 79: Ice accretion variables at altitude 7000 m, flight Mach number 0.6, 25 micron droplet diameter and 10 gm/m^3 LWC.

Figure 80 (a), (b), (c) shows the envelope trajectories, the ice growth with time and the local collection efficiency at a droplet diameter of 50, microns. The envelope trajectories show that most of the impingements locations are in the inside portion of the intake and some of it is above the nose but the outside subjected area is larger than the corresponding case for 0.8 flight Mach number and this can be concluded also from the plot of the local collection efficiency.

(a). The upper and lower envelop of the droplet trajectories

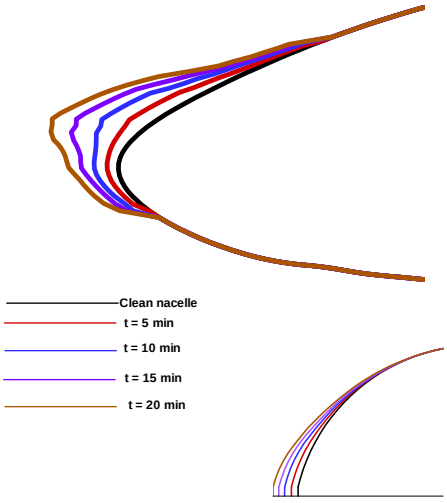

(b). The ice growth

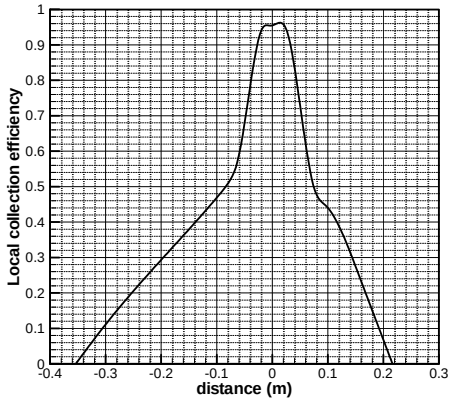

(c). The local collection efficiency for the clean nacelle.

Figure 80: Ice accretion variables at altitude 7000 m, flight Mach number 0.6, 50 micron droplet diameter and 10 gm/m^3 LWC.

In the figure of the local collection efficiency the plot starts at -0.32 approximately and propagates with the positive values which is the inside portion of the intake surface and finally finishes at 0.22 m. In addition there are ice growth on the inside portion of the intake but most of it is happened on the outer surface of the intake as shown in the figure while the ice growth on the boss of the fan is also nearly axi-symmetrical.

Figure 81 (a), (b), (c) shows the envelope trajectories, the ice growth with time and the local collection efficiency at a droplet diameter of 25, microns and Mach number of 0.4. The envelope trajectories show that most of the impingements locations are in the outside portion of the intake and some of it is below the nose and this can be concluded also from the plot of the local collection efficiency. In the figure of the local collection efficiency the plot starts at -0.135 approximately and propagates with the positive values which is the inside portion of the intake surface and finally finishes at -0.065 m. In addition most of the ice growth is taken place on the outside portion of the intake while the ice growth on the nose of the fan is approximately axi-symmetrical.

(a). The upper and lower envelop of the droplet trajectories.

(b). The ice growth

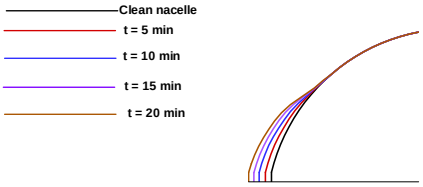

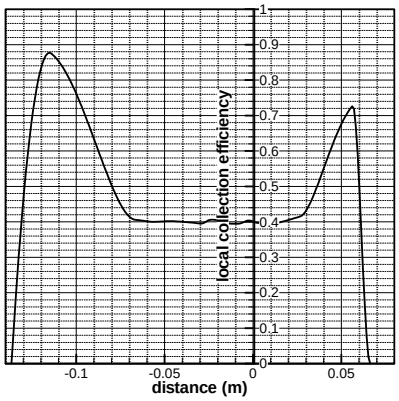

(c). The local collection efficiency for the clean nacelle.

Figure 81: Ice accretion variables at altitude 5000 m, flight Mach number 0.4, 25 micron droplet diameter and 10 gm/m^3 LWC.

Figure 82 (a), (b), (c) shows the envelope trajectories, the ice growth with time and the local collection efficiency at a droplet diameter of 50, microns. The envelope trajectories show that most of the impingements locations are in the outside portion of the intake and some of it is below the nose and this can be concluded also from the plot of the local collection efficiency. In the figure of the local collection efficiency the plot starts at -0.2 approximately and propagates with the positive values which is the inside portion of the intake surface and finally finishes at -0.1 m. In addition most of the ice growth is taken place on the outside portion of the intake while the ice growth on the nose of the fan is approximately axi-symmetrical.

(a) The upper and lower envelop of the droplet trajectories.

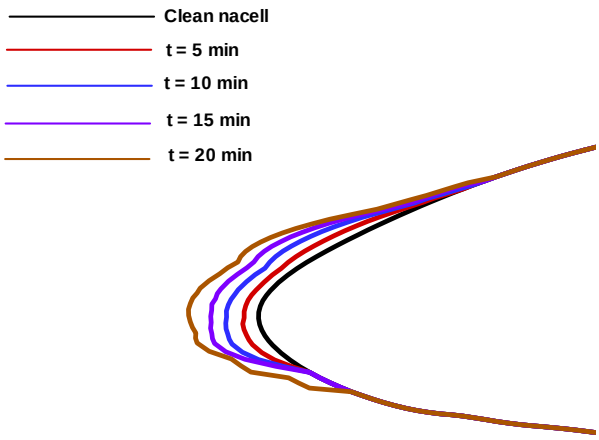

(b). The ice growtn

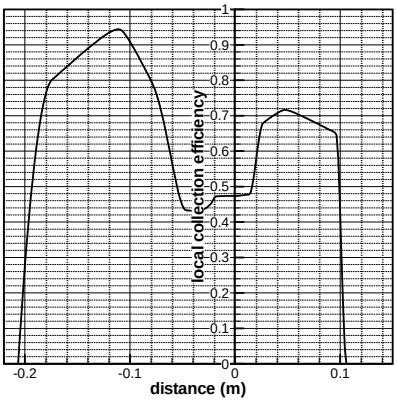

(c). The local collection efficiency for the clean nacelle.

Figure 82: Ice accretion variables at altitude 5000 m, flight Mach number 0.4, 50 micron droplet diameter and 10 gm/m^3 LWC.

Figures 83 and 84, show the icing characteristics for 0.3 flight Mach number and different droplet diameters (15 and 50 microns). Figure 83 (a), (b), (c) shows icing accretion for a droplet diameter of 15, microns. The envelope trajectories show that most of the impingements locations are in the outside portion of the intake as clarified from the plot of the local collection efficiency.

(a). The upper and lower envelop of the droplet trajectories.

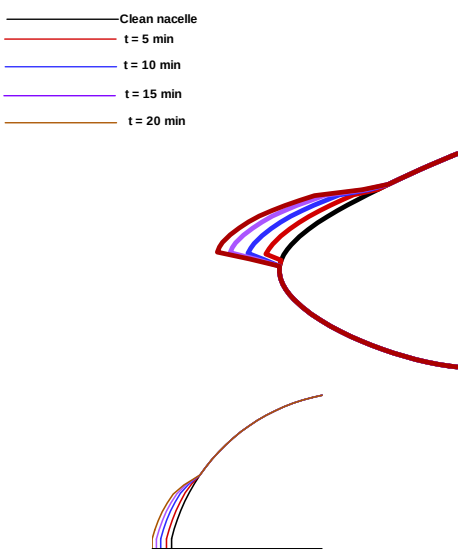

(b). The ice growth

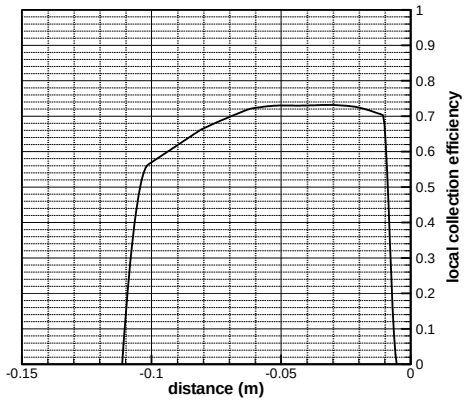

(c). The local collection efficiency for the clean nacelle.

Figure 83: Ice accretion variables at altitude 5000 m, flight Mach number 0.3, 15 micron droplet diameter and 10 gm/m^3 LWC.

Local collection efficiency starts approximately at -0.111, propagates in the outside portion of the intake surface and ends at -0.005 m. Consequently all of the ice growth is taken place on the outside portion of the intake while the ice growth on the nose of the fan is axi-symmetric.

Figure 84 (a), (b), (c) shows icing characteristics of 50, microns droplet. The envelope trajectories show that most of the impingements locations are in the outside portion of the intake, and clarified from local collection efficiency. Local collection efficiency starts at -0.25101 m, propagates outside of the intake surface and finally finishes at 0.02684 m. Consequently all of the ice growth is taken place on the outside portion of the intake while the ice growth on the nose of the fan is approximately axi-**symmetrical**.

(a). The upper and lower envelop of the droplet trajectories.

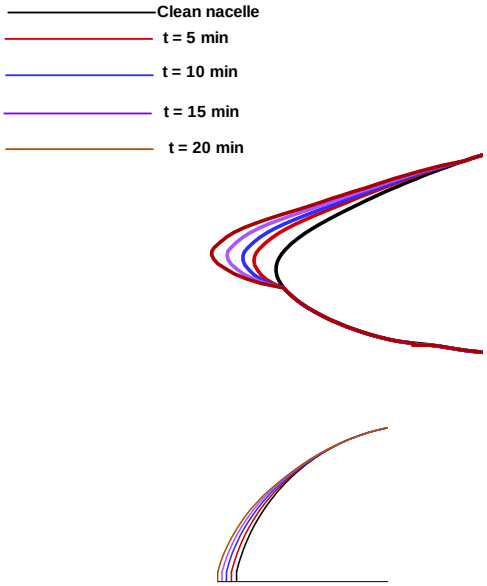

(b). The ice growth

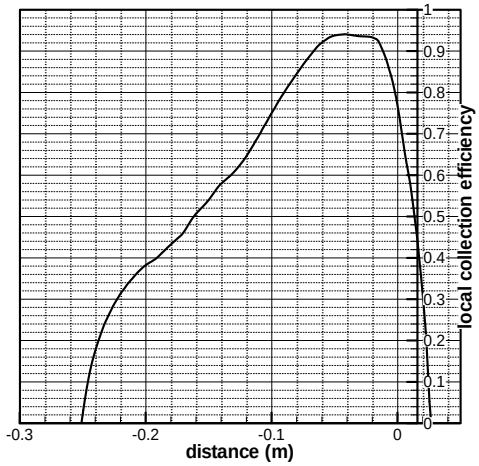

(c). The local collection efficiency for the clean nacelle.

Figure 84: Ice accretion variables at altitude 5000 m, flight Mach number 0.3, 50 micron droplet diameter and 10 gm/m^3 LWC

Figure 85 (a),(b),(c) (d) shows the ice accretion for different droplet diameters 15,25,35,50 microns compared at different flight Mach numbers 0.8,0.6,0.4. Figure (a) compares the variation of the ice accretion shapes at flight Mach number 0.8 which shows that as the droplet size increases the ice thickness and the area of the accretion increases also the ice tends to accrete nearer to the nose as the droplet size increases. Figure (b) compares the variations of the ice accretion shapes at flight Mach number 0.6 which shows that as the droplet size increases the ice thickness and the area of the accretion increases also the ice tends to accrete nearer to the nose as the droplet size increases. Figure (c) compares the variations of the ice accretion shapes at flight Mach number 0.4 which shows that as the droplet size increases the ice thickness and the area of the accretion increases also the ice tends to accrete nearer to the nose as the droplet size increases. Figure (d) compares the variation of the ice mass for 0.8, 0.6, 0.4 flight Mach number for different droplet sizes. In this figure it is illustrated that the accreted mass of ice is increased as the droplet size increases.

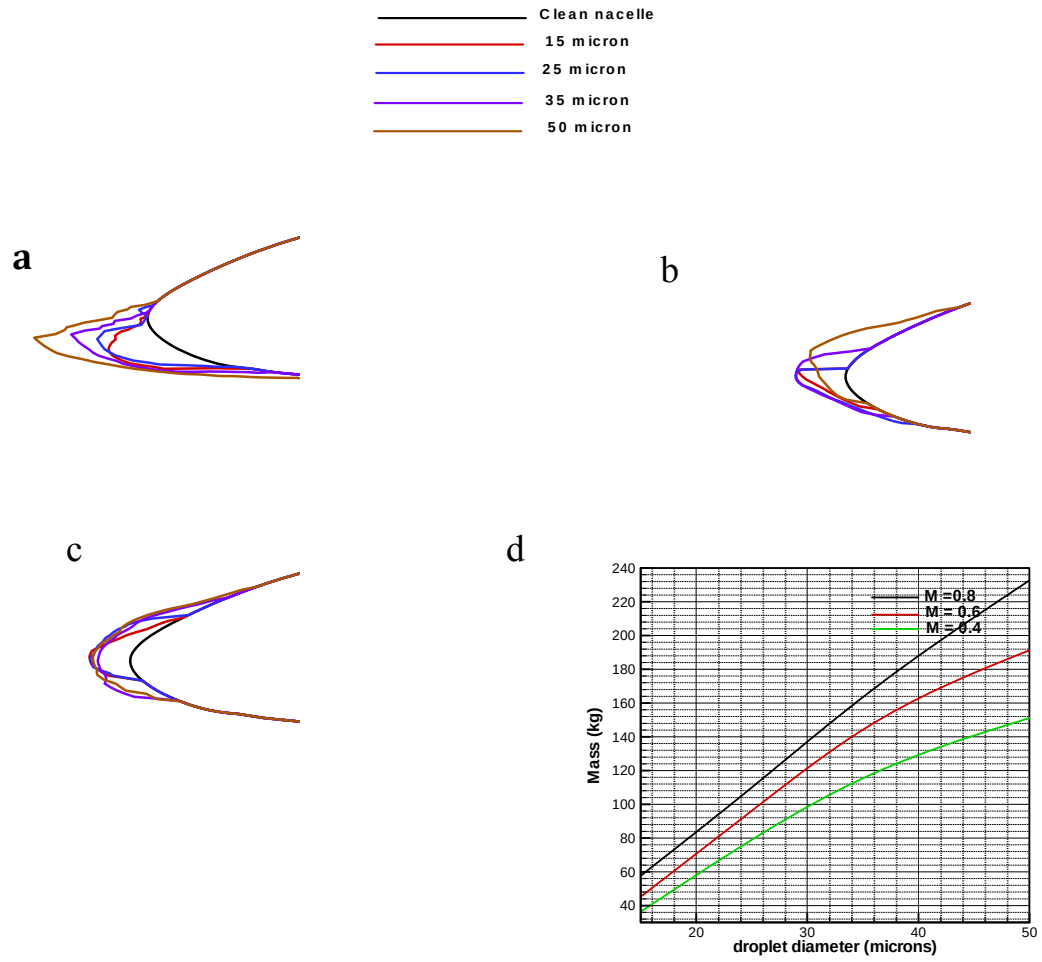

Figure 85: Effect of droplet size on ice accretion for flight altitude 8461m and LWC 10 gm/m^3 at 20 min or each of the following cases: (a) 0.8 Mach number; (b) 0.6 Mach number; (c) 0.4 Mach number; (d) Ice accretion Mass for different Mach number.

Figure 86 (a), (b), (c) shows the effect of droplet size on ice accretion at 0.8, 0.6 and 0.4 flight Mach numbers and sizes vary from 25 to 50 microns.

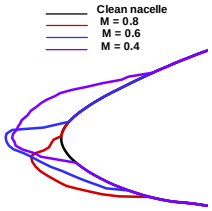

Figure 86a: Effect of Mach number on ice accretion for flight altitude 8461 m, Mach numbers 0.8, 0.6, 0.4, with the same injected rate of water at the far field and 25 micron droplet size at 20 min.

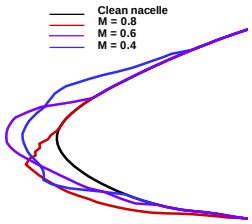

Figure 86b: Effect of Mach number on ice accretion for flight altitude 8461 m, Mach numbers 0.8, 0.6, 0.4 with the same injected rate of water at the far field and 35 micron droplet size at 20 min.

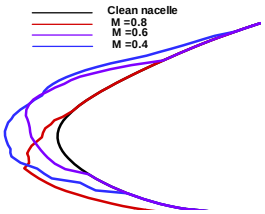

Figure 86c: Effect of Mach number on ice accretion for flight altitude 8461 m, Mach numbers 0.8, 0.6, 0.4, and with the same injected rate of water at the far field and 50 micron droplet size at 20 min.

Figure 87 (a), (b), (c) shows the variations of mass of the accreted ice with time for 25, 35, and 50 droplet diameters at 0.8, 0.6, and 0.4 flight Mach numbers respectively with the same rate of water injection at the far field. These figures show that the lower the Mach the higher the rate of ice accretion. Also as the droplet size increases, the rate of ice accretion increases also.

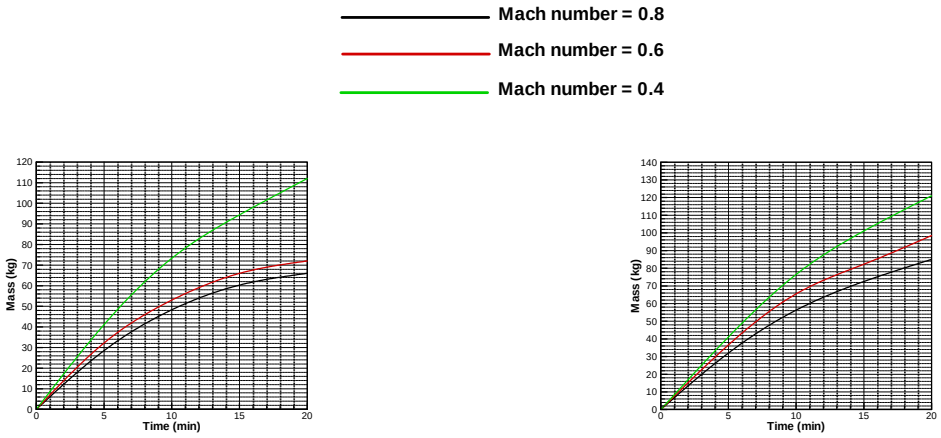

Figure 87a: The mass of accreted ice on the nacelle with time for droplet diameter 25 micron, with the same injected rate of water at the far field.

Figure 87b: The mass of accreted ice on the nacelle with time for droplet diameter 35 micron, with the same injected rate of water at the far field.

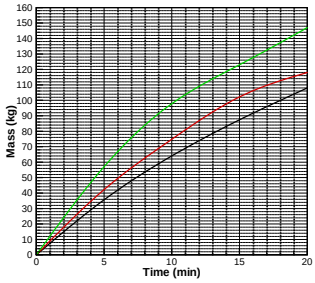

Figure 87c: The mass of accreted ice on the nacelle with time for droplet diameter 50 micron, with the same injected rate of water at the far field.

Figure 88 shows the effect of the LWC on the ice accretion, for 25 micron droplet diameter, and 0.8 flight Mach number at 8461.5 m altitude. It is evident from this figure that as the LWC increases the ice thickness increases.

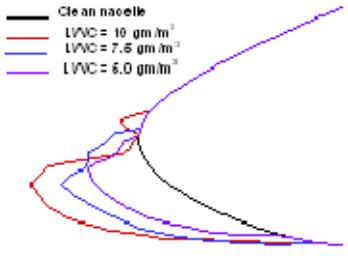

Figure 88: Effect of LWC on ice accretion for flight altitude 8461 m, Mach numbers 0.8, and LWC 5,7.5,10 gm/m3 respectively and 25 micron droplet size at 20 min.

Figure 89 shows the variations of the mass of accreted ice with time for droplet diameter 25 micron, for flight altitude 8461 m, Mach numbers 0.8, and LWC 5, 7.5, 10 gm/m^3 respectively. It obvious that as the LWC values increases the rate of the accreted ice mass is increased.

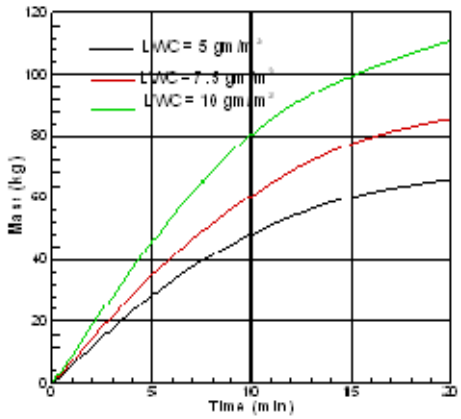

Figure 89: The mass of accreted ice on the nacelle with time for droplet diameter 25 micron, for flight altitude 8461 m, Mach numbers 0.8, and LWC 5, 7.5, 10 gm/m3 respectively.

4.4 Aerodynamic Degradation

The ice accretion of aircraft components such as wings and engines intakes has a sever effect on the aircraft performance and reduces the safety margins as mentioned by the FAA [72]. Herein in this chapter the various effects due to the ice accretion on the intake of a high by-pass ratio (CF-6) engine intake are introduced and studied. These effects are the changes of the drag coefficient, temperature inlet flow distortion, pressure inlet flow distortion, ratio of mass flow rate relative to the corresponding design mass flow rate and the changes of the velocity profiles with time due to ice accretion. Both the changes of the drag coefficient and mass flow rate has a great effect on the engine thrust certainly, and both the changes of the temperature inlet flow distortion and pressure inlet flow distortion, at the same time has a great effect on the performance of the transonic fan.

4.5 Results and Discussion

Figure 90 through 92 illustrates the changes of the drag coefficient with time of the iced intake for 15, 25, 35, 50 micron droplet diameter, at 8461.5 m, altitude and 0.8, 0.6, 0.4 flight Mach numbers respectively. Figure 90 shows that the drag coefficient decreases with time due to ice accretion. The change of the intake shape increases the flow separation on the outer surface of the intake and more transonic bubbles appears. In addition the growth direction as mentioned in chapter (4) is inward, which reduces the intake inlet area and consequently reduces the mass flow rate as will be mentioned in the following, which increases the adverse pressure gradient slightly on the inner surface and hence the drag force is decreased. Figures 91 and 92 shows that drag coefficient increases with time due to ice accretion. This increase in drag for the case of flight Mach number 0.6 is due to increase of the mass flow rate through the intake. This increase reduces the adverse pressure gradient on the inner surface of the intake, and hence the drag is increased. For the case of 0.4 flight Mach number the drag coefficient is increased slightly because of the increase in the cross section of the intake cowl due to ice built up.

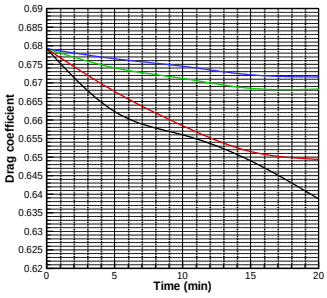

Figure 90:The variation of the drag coefficient with time for 15, 25, 35, 50 microns droplet diameter at 0.8 flight Mach number.

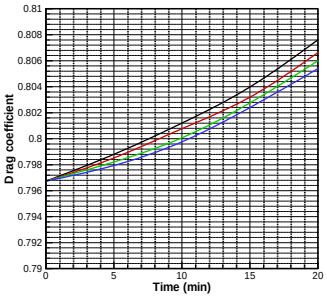

Figure 91: The variation of the drag coefficient with time for 15, 25, 35, 50 microns droplet diameter at 0.6 flight Mach number.

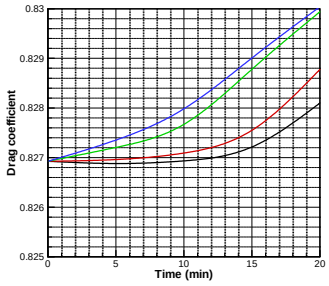

Figure 92: The variation of the drag coefficient with time for 15, 25, 35, 50 microns droplet diameter at 0.4 flight Mach number.

Figure 93 through 95 illustrates the changes of the ratio of the mass flow rate with respect to the corresponding design mass flow rate (mass flow rate ratio) with time of the iced intake for 15, 25, 35, 50 micron droplet diameter, at 8461.5 m, altitude and 0.8, 0.6, 0.4 flight Mach numbers respectively. Figure 93 shows that the mass flow rate ratio decreases with time due to ice accretion. While figure 94 shows that the mass flow rate ratio increases with time due to ice accretion and figure 95 show that the mass flow rate ratio decreases with time due to ice accretion but these changes of mass flow rate ratio are very small and can be negligible.

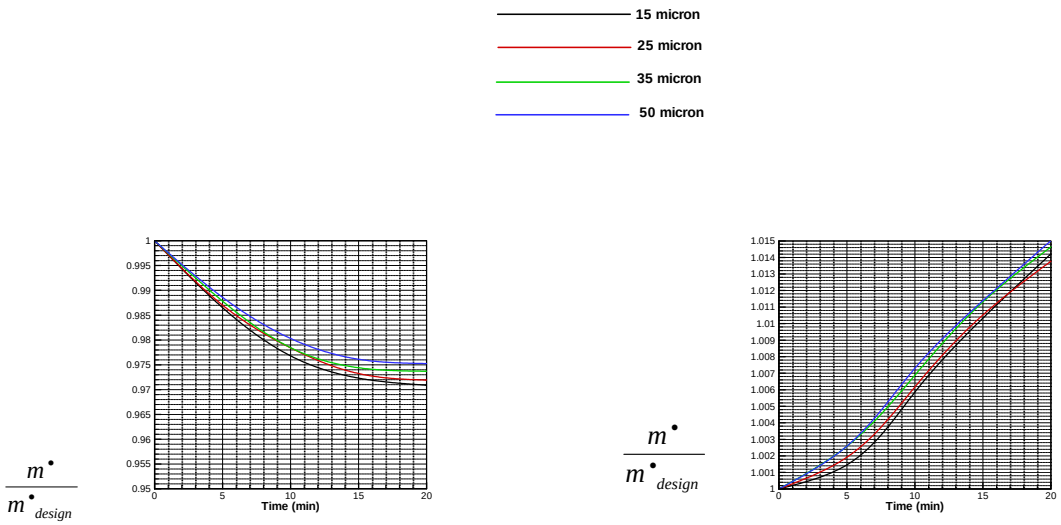

Figure 93: The variation of the mass flow ratio of air with time for 15, 25, 35, 50 microns droplet diameter at 0.8 flight Mach number.

Figure 94: The variation of the mass flow ratio of air with time for 15, 25, 35, 50 microns droplet diameter at 0.6 flight Mach number.

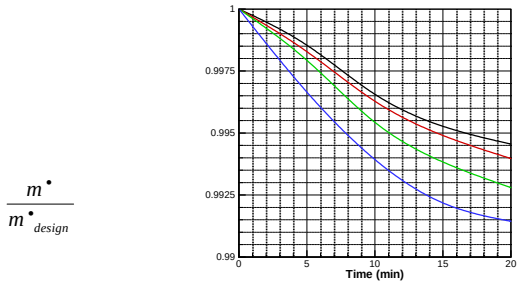

Figure 95: The variation of the mass flow ratio of air with time for 15, 25, 35, 50 microns droplet diameter at 0.8 flight Mach number.

Figure 96 through 98 illustrates the changes of velocity magnitude with time of the iced intake for 15, 25, 35, 50 micron droplet diameter, at 8461.5 m, altitude and 0.8, 0.6, 0.4 flight Mach numbers respectively at various locations inside the intake. These figures shows that the velocity magnitude decrease with time with respect to that of the clean nacelle at 0.8 flight Mach number, while its values increases slightly with time at 0.6 flight Mach number. For 0.4 flight Mach number there are no remarkable changes for the velocity magnitude.

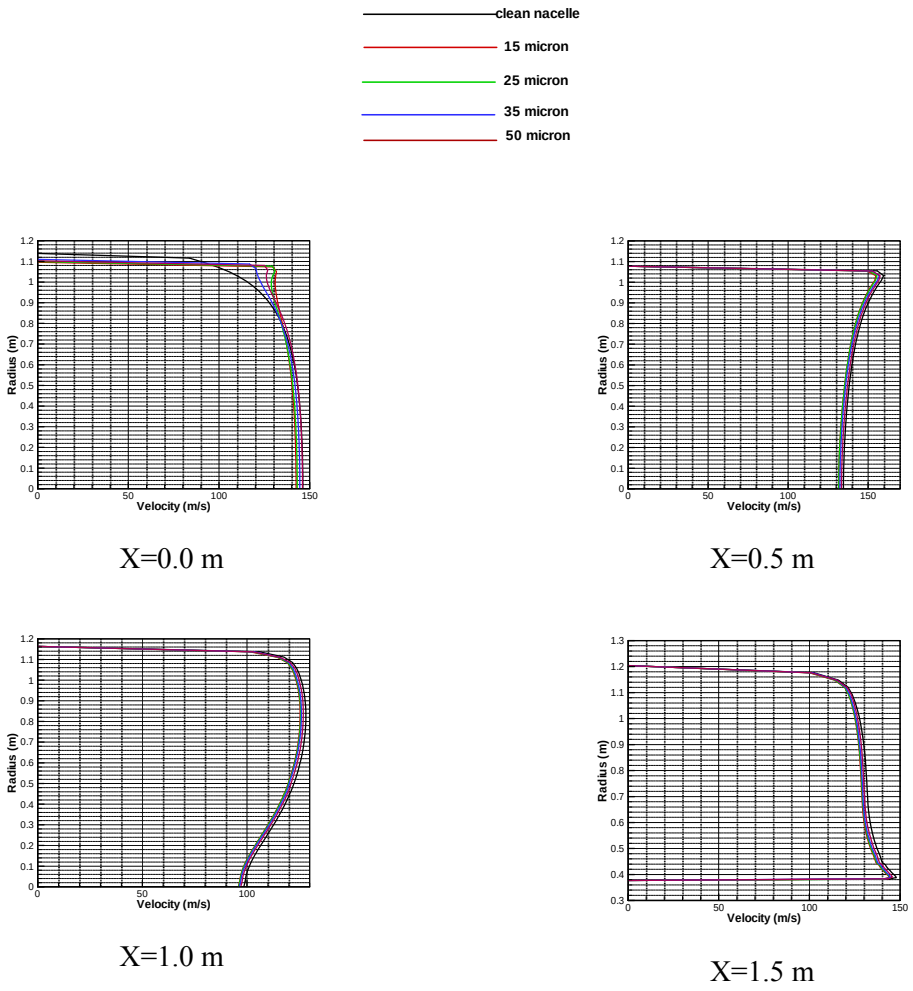

Figure 96: The velocity distribution at different axial locations from the intake nose for 0.8 flight Mach number.

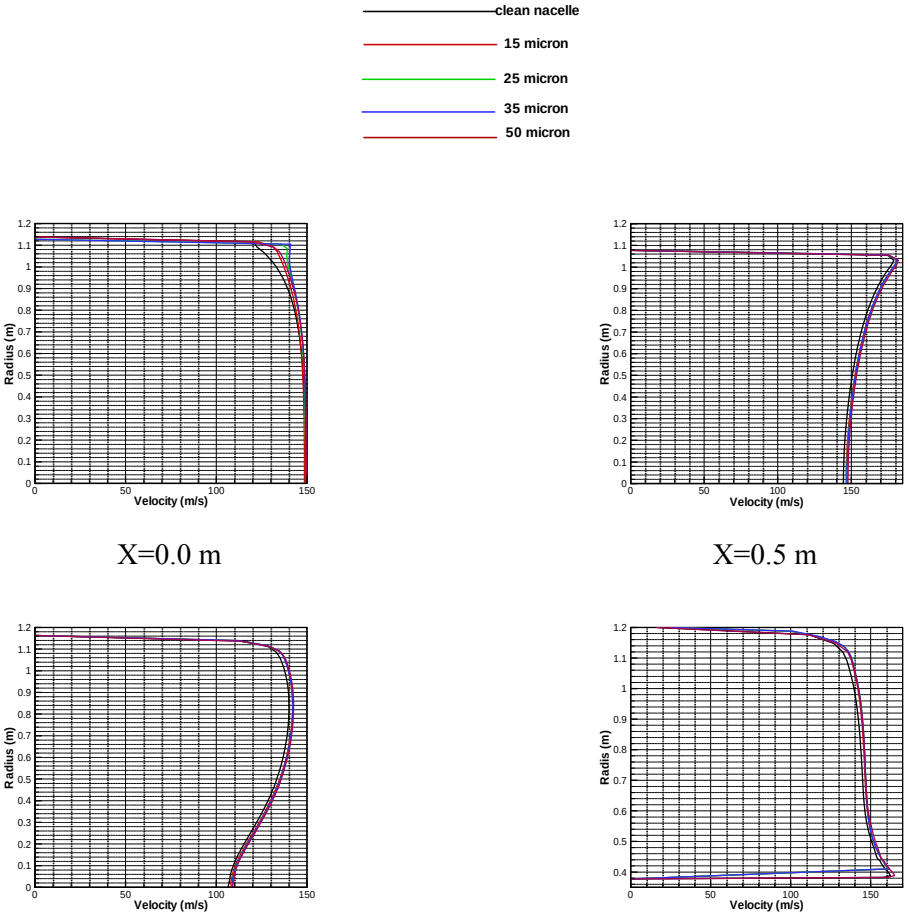

Figure 97: The velocity distribution at different axial locations from the intake nose for 0.6 flight Mach number.

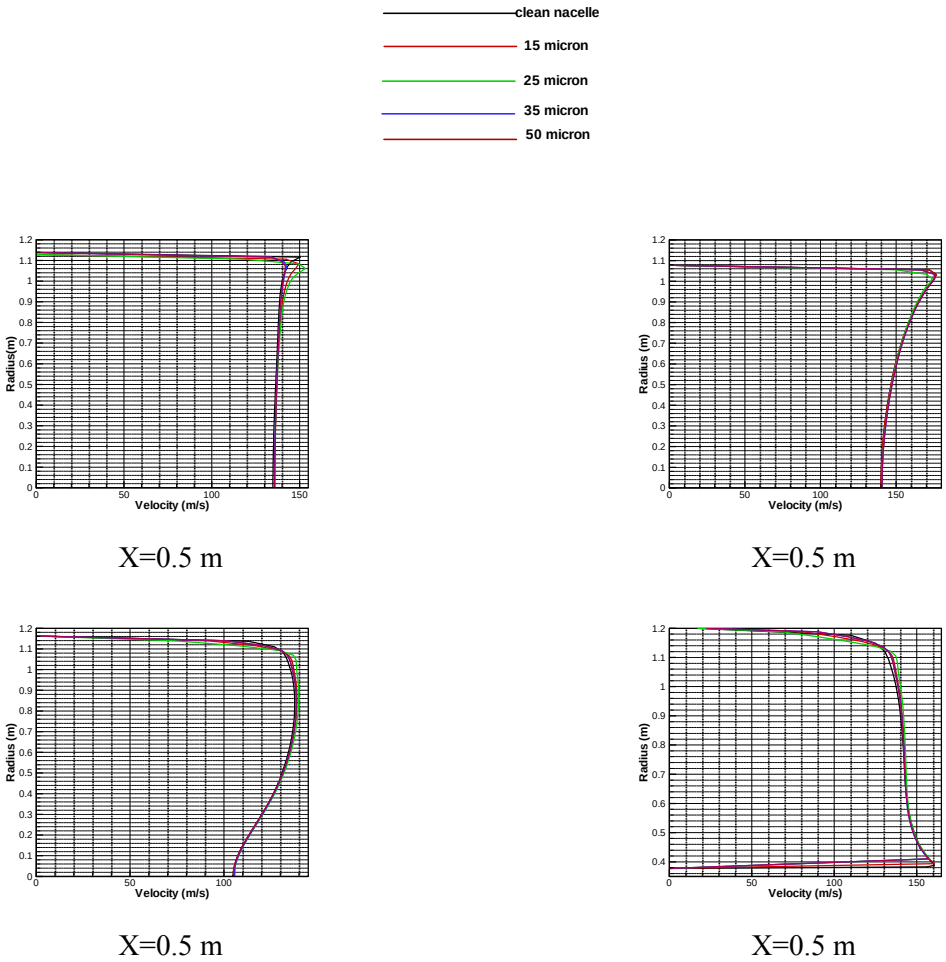

Figure 98: The velocity distribution at different axial locations from the intake nose for 0.4 flight Mach number.

Figures 99 through 102 show the variations of the pressure recovery factor, which is defined as the ratio of total pressure at the fan inlet to the total pressure at the far field, with time due to ice accretion for different droplet sizes (15, 25, 35, 50 microns). All of these figures illustrate that the pressure recovery factor is altered because of the intake shape variations and the formed roughness due to rime ice growth. Figure 99 show the pressure recovery factor for 0.8 flight Mach number, where the values of PRF starts at 0.98 for all droplet diameters and decreases to 0.96 for the case of droplet size 15 micron and 0.94 for the case of 50 micron droplet size. This is because of the inward ice growth for all droplet size at 0.8 flight Mach number. For the case of 0.6 flight Mach number the values decreases to 0.977 for the case of 15 micron droplet size and 0.97 for the case of 50 micron droplet size and the same situation is for 0.4 flight Mach number, while for 0.3 flight Mach number there is no considerable changes in the PRF values with time because of the outside ice growth for that case which does not affect the flow in the intake.

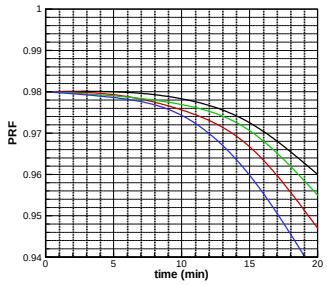

Figure 99: The PRF (pressure recovery factor) variation with time due to ice accretion for 0.8 flight Mach number and 0.1141 corrected mass flow rate.

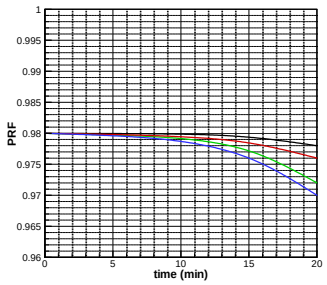

Figure 100: The PRF (pressure recovery factor)variation with time due to ice accretion for 0.6 flight Mach number and 0.1141 corrected mass flow rate.

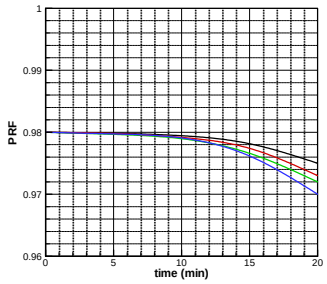

Figure 101: The PRF (pressure recovery factor)variation with time due to ice accretion for 0.4 flight Mach number and 0.1141 corrected mass flow rate.

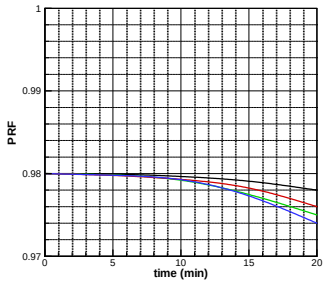

Figure 102: The PRF (pressure recovery factor)variation with time due to ice accretion for 0.3 flight Mach number and 0.1141 corrected mass flow rate.

Figures 103 through 106 show the variations of IFD (inlet flow distortion) percent which is defined as the ($\frac{P_{\max} - P_{\min}}{P_{av}}$) with time due to ice accretion for different droplet sizes (15, 25, 35, 50 microns). Figure 103 show the IFD % for 0.8 flight Mach number, where its value starts at 2.5 and increases to 2.6 for the case of droplet size 15 micron and 3.35 for the case of 50 micron droplet size. For the case of 0.6 flight Mach number the values starts at 4.01and increases to 4.12 for the case of 15 micron droplet size and 4.23 for the case of 50 micron droplet size as shown in figure 104. For the case of 0.4 flight Mach number the values starts at 5.52and increases to 5.7 for the case of 15 micron droplet size and 6.48 for the case of 50 micron droplet size as shown in figure 105. For the case of 0.3 flight Mach number the values starts at 6.12and increases to 6.1255 for the case of 15 micron droplet size and 6.18 for the case of 50 micron droplet size as shown in figure 106.

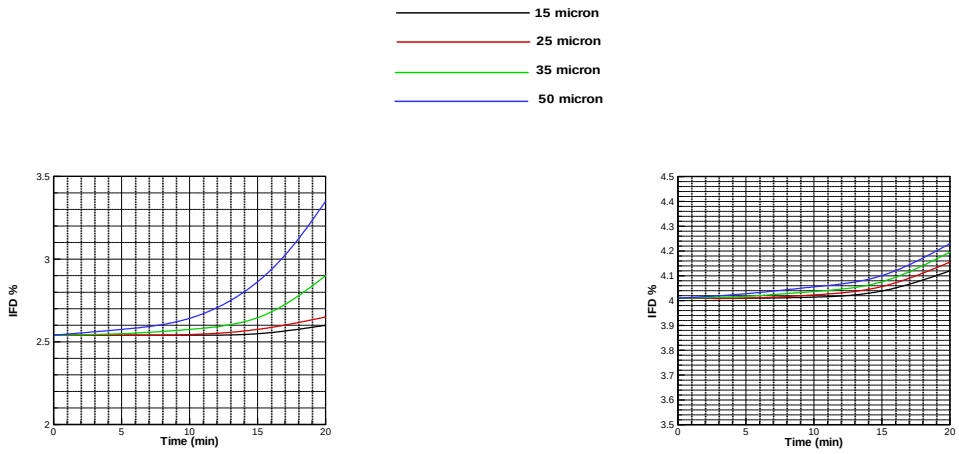

Figure 103: The IFD (inlet flow distortion) variation with time due to ice accretion for 0.8 flight Mach number and 0.1141 corrected mass flow rate.

Figure 104: The IFD (inlet flow distortion) variation with time due to ice accretion for 0.6 flight Mach number and 0.1141 corrected mass flow rate.

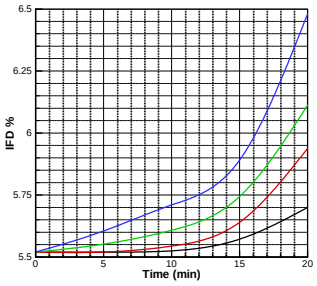

Figure 105: The IFD (inlet flow distortion) variation with time due to ice accretion for 0.4 flight Mach number and 0.1141 corrected mass flow rate.

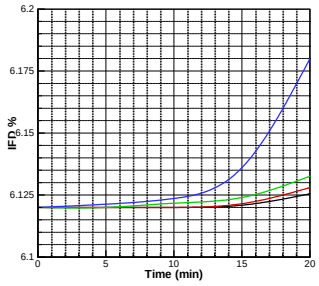

Figure 106: The IFD (inlet flow distortion) variation with time due to ice accretion for 0.3 flight Mach number and 0.1141 corrected mass flow rate.

6.0 CONCLUSION

This work examined the subsonic flow in an intake of the high by-pass ratio (HBPR) turbofan engine (examples; GE CF-6, CFM56, PW4000, RR Trent) and the associated ice accretion on it. The intake performance degradation due to ice was studied as well. In this work, four topics were treated, namely:

- Air flow analysis upstream and through the intake.
- Water droplets trajectories simulation.
- Local collection efficiency analysis.
- Variation of ice accretion with time
- Aerodynamic degradation due to ice accretion and roughness.

6.1 Conclusions of Air Flow Analysis

Numerical simulation for the air flow field upstream and through the intake of a high bypass ratio turbofan engine is carried out using the commercial code Fluent 6.0. The flow field is treated as a three dimensional, compressible, and turbulent flow where Navier-Stokes equations together with the Spalart-Allmaras turbulence model were solved for both cruise and takeoff conditions. The physical domain boundaries are taken six times the intake diameter at the fan face as recommended by "FLUENT.INC" to get up a satisfactory results. The generate domain is a 3D sector including the intake inside it which is considered the computational domain. A hexagonal mesh element is generated in the computational domain because this type is considered computationally fast, and the solution convergence is reached quickly. The mass flow rate through the intake for different altitudes and flight Mach number is obtained from the CF-6 engine manual.

The following conclusions are obtained

1. The air flow characteristics such as static-to-total pressure and temperature through a subsonic intake are a function only in:
   - Flight Mach number - Mass flow parameter
   It is independent of the flight attitude.
2. A transonic bubbles is formed on the outside portion of the intake just behind the intake lip for high flight Mach number (M>0.4)
3. For flight Mach number higher than critical Mach number which is corresponding to Area ratio of unity ($\frac{A_i}{A_\infty}$), most of the compression of the air is carried out externally.
4. For flight Mach number lower than critical Mach number air is accelerated upstream intake and then compressed inside the inlet
5. For the case of takeoff the flow upstream the intake is accelerated (i.e. external expansion) and then inside the intake at 1.0 m from the intake nose the flow is decelerated till the fan face.
6. There for the intake at flight Mach numbers higher that the critical Mach number which is corresponding to Area ratio of unity ($\frac{A_i}{A_\infty}$), works like a diffuser, and for values lower than this critical Mach number works like a nozzle.

6.2 Droplet Trajectories and Ice Accretion

Regarding to ice accretion process, the effects of droplet size, flight Mach number on local collection efficiency and frozen fraction were investigated.

The droplet diameters of 15, 25, 35, 50 microns were employed

Cases of flight Mach numbers of 0.8, 0.6, 0.4, and 0.3 were examined

The following conclusions are found

1. Droplet trajectory depends mainly on its size and flight Mach number which influenced local collections efficiency
2. Time step value affects ice accretion shape, and as its value decreases the more accurate ice shape is obtained.

3. Although the value of the time step affects the ice accretion shape, the flow through the intake is almost unaffected by the time step value because the ice shape variations is negligible with respect to intake diameter.
4. As the droplet diameter is increased the impingement area is increased and hence the rate of ice accretion is increased.
5. For flight Mach number of 0.8 and mass flow parameter of 0.0304, impingements occurred on the pressure side of inlet (inside portion of the intake lip) while for 0.6 flight Mach number and same mass flow parameter, the impingements were nearly symmetrical around the both lip surface.
6. For 0.8 flight Mach number the ice growth was noticed on the inside portion of the intake, while for 0.6 flight Mach number the ice growth was symmetrical but for the droplet size 50 micron most of it was on the outside portion
7. Impingement at both 0.4 and 0.3 Mach numbers and mass flow parameter of 0.0304 occurred on the outside portion of the intake.
8. For 0.4 and 0.3 flight Mach number most of the ice growth was on the outside portion of the intake.
9. For small droplet diameter 15 microns the impingement area and hence the subjected area for ice accretion is small, while for large droplet diameters such as 50 microns the impingement area is large. This means that for the large droplet diameters the rate of ice accretion is increased.
10. For the same injected rate of supercooled water droplets at the far field the inlet, ice accretion is higher for the low Mach number such as 0.4 Mach number compared with high Mach number such as 0.8 Mach number.

6.3 Aerodynamic Degradation

The flow through the intake is affected by any changes in its shape due to ice accretion when the aircraft is passing through clouds. The important properties such as drag coefficient, mass flow rate, radial velocity distribution and diffuser PRF (pressure recovery factor) for the same fan rotational speed were investigated.

The following conclusions are extracted.

1. The drag coefficient is decreased for 0.8 flight Mach number with time due to ice accretion because the mass flow rate was decreased with time.
2. The drag coefficient is increased for 0.6 flight Mach number with time due to ice accretion, slightly because the mass flow rate is increased with time.
3. The drag coefficient is increased for 0.4 flight Mach number with time due to ice accretion, slightly because of the increasing transonic bubbles on the outside surface of the intake.
4. For 0.8 flight Mach number the mass flow rate is decreased with time due to ice accretion, while for 0.6 flight Mach number the mass flow rate is increased with time.
5. The intake pressure recovery factor (PRF) is changed due to ice accretion for 0.8 and 0.6 flight Mach numbers, while for 0.4 and 0.3 the was no significant changes in the intake pressure recovery factor (PRF).

6.4 Future Work

To enhance the predictive methodologies of the ice accretion on the intake of a high by-pass ratio turbofan engine as presented in this work, further improvement to the computational model should be made. The following points warrant further development in future work with some relevant experimental investigations:

1. Solving the generated vortices unsteadiness with the large eddy simulation turbulence technique.
2. Developing the computational procedure to predict the ice accretion unsteadily rather than quasi-steadily.
3. Developing the computational model the run back due to shear stress of the unfrozen quantity of incoming water droplets.
4. Modeling of de-icing and ice shedding from the intake surface which may cause foreign object damage to the fan (FOD).

7.0 REFERENCES

1. Gobran, M.H. Analytical Approach To Turbofan Engine Modeling, Control And Non-Linear Simulation. Ph.D. Thesis, Cairo University, 1995.

2. Fluent Documentation, User Guide Manual

3. Hansman, et al. Comparison of Wet and Dry Growth in Artificial and Flight Icing Conditions. Paper 86-1352 at AIAA/ASME 4th thermophysics and heat transfer conference Boston June 1986 .

4. Bragg M.B. Rime Ice Accretion and Its Effect on Airfoil Performance. Ph.D. Dissertation, The Ohio State University, 1981 and NASA CR 165599, 1982

5. Papadakis M, Alansatan S, Yeong HW. Aerodynamic Performance of a T-tail with Simulated Ice Accretions. AIAA Paper 2000-0363, 2000

6. Lee S, Dunn T, Gurbacki H, Bragg MB, Loth E. An Experimental and Computational Investigation of span-wise step-ice shapes on airfoil aerodynamics. AIAA Paper 98-0490, 1998.

7. Zaman K., Potapczuk M.G. The Low Frequency Oscillation in the Flow Over a NACA Airfoil with an Iced leading edge. Mueller TJ, editor. Low Reynolds number aerodynamics. New York: Springer, 1989. P.271–82.

8. Mund, M. G., and Guhna, H., "Gas Turbine Dust Air Cleaners," American Society of Mechanical Engineers, Paper 70-GT-104, Aug. 1970.

9. Sirs, R. C., "The Operation of Gas Turbine Engines in Hot & Sandy Conditions-Royal Air Force Experiences in the Gulf War," AGARD-CP-558, Paper No. 2, May 1994.

10. Grant, G., "A Model To Predict Erosion In Turbomachinery Due To Solid Particles In Particulate Flow", Ph. D. Dissertation , Univ. of Cincinnati, 1973.

11. Montgomery, J. E., and Clark, J. M., Jun., "Dust Erosion Parameters for a Gas Turbine," Soc. of Automotive Engineers Summer Meeting, 1962, Preprint 538A

12. Tabakoff W., Hamed A., Metwally M., " Effect Of Particle Size Distribution On Particle Dynamics And Blade Erosion In Axial Flow Turbines," J. Engineering For Gas Turbines And Power , October 1991 , Vol. 113

13. Hamed, A., Tabakoff, W., Richard B. Rivir, Kaushik Das, and Puneet Arora, " Turbine Blade Surface Deterioration By Erosion", Journal of Turbomachinery- July 2005- Vol. 127, Issue 3, pp. 445-452.

14. Japikse, D., "Review- Progress in Numerical Turbo-machinery Analysis" ASME J. of Fluids Engineering, pp 592-606, (1976).

15. Wulf, R.H., Kramer, W.H., and Paas, J.E., "CF6-6D Jet Engine Performance Deterioration" NASA/CR-159786, NASA, (1980).

16. Peterson, R.C., "Design Features for Performance Retention in the CFM56 Engine " Turbo-machinery Performance Deterioration FED - Vol. 37 the AIAA/ASME 4th Joint Fluid Mechanics Plasma Dynamics and Lasers Conference, Atlanta, Georgia, (1986).

17. Elsayed Abdel Azim, A.F., and Brown, A., "Computer Prediction of Erosion Damage in Gas Turbine" ASME Paper 87-GT-127, 32nd ASME Int. Gas Turbine Conf., California, USA, (1987).

18. Clevenger, W.B., Jr., and Tabakoff, W., "Similarity Parameters for Comparing Erosive Particle Trajectories in Hot Air and Cold Air Radial Inflow Turbines" ASME Paper 74-GT-65, (1974).

19. Elsayed Abdel Azim, A.F., and Rashed, M.I.I., "Erosion in Centrifugal Compressors" Paper No.55, Proc. 5th Int. Conf. on Erosion by Liquid and Solid Impact (ELSI V), Newnham Collage, Cambridge Univ., Uk, (1979).

20. Elsayed Abdel Azim, A.F., and Rashed, M.I.I., "Computation of Gas Flow in Centrifugal Compressors Used in Helicopters." Proc. of 5th Int. symposium on Air Breathing Engines, Bangalore, India, 1980.

21. Elsayed Abdelazim, A.F., and Rouleau, W.T., "Three Dimensional Viscous Particulate Flow in a Typical Turbo-expander" Int. J. of Energy Systems, Vol.5, No.2, (1985a)

22. Elsayed Abdel Azim, A.F., "Aerodynamics/Aero-elastic Behavior of Eroded Axial Turbines" 2nd Int. Symposium on Transport Phenomena, Dynamics and Design of Rotating Machinery, Honolulu, Hawaii, USA, (1988)

23. Hassan Zoheir , Particulate flow and Erosion of the Intakes of Turbofan Engines, M. Sc. Thesis, Mr., 2005, Zagazig univ.

24. Elsayed, A.F., Gobran, M.H and Zoheir, H., Erosion damage of axial fan of a HBPR turbofan engine due to sand particles ingestion, Ain Shams Journal of Mechanical Engineering (ASJME), October 2011

25. Dunn, M.G., Padova, C., Moller, J.E., and Adams, R.M., "Performance Deterioration of a Turbofan and a Turbojet Engine upon Exposure to a Dust Environment" ASME Journal of Engineering for Gas Turbine and Power, Vol. 109, pp 336 -343, (1987).

26. Mason, J., Engine Power Loss in Ice Crystal Conditions, Aero Magazine, QTR_4 1 07.